

# OSSEs for an Ensemble 3DVAR Data Assimilation System with Radar Observations of Convective Storms

JIDONG GAO

*NOAA/National Severe Storms Laboratory, Norman, Oklahoma*

CHENGHAO FU

*Hunan Meteorological Bureau, Changsa, Hunan, China, and Cooperate Institute for Mesoscale Meteorological Studies, University of Oklahoma, Norman, Oklahoma*

DAVID J. STENSRUD

*Department of Meteorology, The Pennsylvania State University, University Park, Pennsylvania*

JOHN S. KAIN

*NOAA/National Severe Storms Laboratory, Norman, Oklahoma*

(Manuscript received 16 October 2015, in final form 3 March 2016)

## ABSTRACT

An ensemble of the three-dimensional variational data assimilation (En3DA) method for convective-scale weather has been developed. It consists of an ensemble of three-dimensional variational data assimilations and forecasts in which member differences are introduced by perturbing initial conditions and/or observations, and it uses flow-dependent error covariances generated by the ensemble forecasts. The method is applied to the assimilation of simulated radar data for a supercell storm. Results indicate that the flow-dependent ensemble covariances are effective in enabling convective-scale analyses, as the most important features of the simulated storm, including the low-level cold pool and midlevel mesocyclone, are well analyzed. Several groups of sensitivity experiments are conducted to test the robustness of the method. The first group demonstrates that incorporating a mass continuity equation as a weak constraint into the En3DA algorithm can improve the quality of the analyses when radial velocity observations contain large errors. In the second group of experiments, the sensitivity of analyses to the microphysical parameterization scheme is explored. Results indicate that the En3DA analyses are quite sensitive to differences in the microphysics scheme, suggesting that ensemble forecasts with multiple microphysics schemes could reduce uncertainty related to model physics errors. Experiments also show that assimilating reflectivity observations can reduce spinup time and that it has a small positive impact on the quality of the wind field analysis. Of the threshold values tested for assimilating reflectivity observations, 15 dBZ provides the best analysis. The final group of experiments demonstrates that it is not necessary to perturb radial velocity observations for every ensemble member in order to improve the quality of the analysis.

## 1. Introduction

Many studies have been performed using Doppler radar observations to initialize convection-allowing numerical models (CAMs) with advanced data assimilation

(DA) methods, such as three- or four-dimensional variational techniques (3DVAR or 4DVAR, respectively) and the ensemble Kalman filter (EnKF; Stensrud et al. 2013; Sun et al. 2014). Among these methods, 3DVAR is the least complex approach. It can be modified easily to use mass continuity and other appropriate model equations as weak constraints, and it is so computationally efficient that it has been implemented in real-time applications (Gao et al. 1999, 2004; Barker et al. 2004; Xiao et al. 2005; Hu et al. 2006; Hu and Xue 2007; Ge and Gao

---

*Corresponding author address:* Dr. Jidong Gao, NOAA/National Severe Storms Laboratory, National Weather Center, 120 David L. Boren Blvd., Norman, OK 73072.  
E-mail: jidong.gao@noaa.gov

2007; Ge et al. 2010; Stensrud and Gao 2010; Xie et al. 2011; Gao et al. 2013a). For example, the Advanced Regional Prediction System (ARPS) 3DVAR system with incremental analysis updating was developed at the Center for Analysis and Prediction of Storms (CAPS) specifically to assimilate radar data and other conventional and remotely sensed data into CAMs (Gao et al. 1999, 2004). The system has used WSR-88D data to provide initial conditions for CAM ensemble forecasts during the Hazardous Weather Testbed (HWT) Spring Forecasting Experiments since 2008 (Clark et al. 2012). The ARPS 3DVAR has been also used in the HWT Experimental Warning Program to provide a real-time convective-scale three-dimensional storm analysis (Gao et al. 2013a). Forecasters using these analyses in warning-decision processes found the products had high potential for positive impact on warning operations (Smith et al. 2014; Calhoun et al. 2014).

The more advanced 4DVAR incorporates the full prediction model into the assimilation system and implicitly includes the effects of flow-dependent error covariances through the forward and backward models. Convective-scale radar DA using 4DVAR has been applied successfully to many storm events (Sun and Crook 1997, 1998, 2001; Sun 2005; H. Wang et al. 2013; Sun and Wang 2013). In a recent study, a 4DVAR with radar DA capability was developed for CAMs (H. Wang et al. 2013), and testing indicated that the 4DVAR can lead to significantly improved quantitative precipitation forecasts (QPFs) compared to the 3DVAR system. Chang et al. (2015) reported on the implementation of an ice-phase microphysical process in a convective-scale 4DVAR and found that using this scheme had positive impacts on the short-term forecasts. However, despite these encouraging results, more work is needed for convective-scale 4DVAR when used with more complex microphysics schemes.

Encouraging results also have been obtained using the EnKF method to assimilate radar observations of convective storms. Typically, one of two general types of EnKF systems is used in convective-scale applications. One is the ensemble square root filter (EnSRF; Whitaker and Hamill 2002; Snyder and Zhang 2003; Zhang et al. 2004; Tong and Xue 2005; Dowell et al. 2004, 2011; Yussouf and Stensrud 2010; Marquis et al. 2014), while the other is the local ensemble transform Kalman filter (Hunt et al. 2007; Thompson et al. 2014). Recent radar DA experiments by Thompson et al. (2014) suggested that there was no significant difference between the two EnKF schemes and both were equally capable for radar DA.

The relative advantages and disadvantages of variational and EnKF approaches to DA were extensively

discussed by Lorenc (2003) and Kalnay et al. (2007). While the 3DVAR is easy to implement and computationally efficient, its major shortcoming is having stationary and isotropic background error covariances, which is not optimal for the high spatial and temporal intermittency of convective-scale flows. In 4DVAR, the background error covariance is propagated implicitly in a dynamically consistent manner by the interactions with the numerical weather prediction (NWP) model, its adjoint model, and observation operators, but the development of the adjoint model is time consuming, and any updates to the numerical model require an update to the adjoint model. One of the advantages of the EnKF over variational methods is that the former can explicitly provide the flow-dependent background error covariances. However, a major shortcoming with ensemble-based DA is rank deficiency or sampling error as a result of relatively small ensemble sizes. This problem may be even more severe with convective-scale DA because large model biases may exist and the total number of degrees of freedom of the system is much larger than that for synoptic scale. Caya et al. (2005) found that EnKF typically produces better analyses than 4DVAR in later assimilation cycles, but EnKF has a spinup problem during early assimilation cycles.

In addition, the model states resulting from applying the EnKF method usually are not balanced, and this lack of balance sometimes leads to the model forecasts moving quickly away from the analyses, whereas balance constraints can be imposed with 3DVAR and 4DVAR.

To blend the advanced features of both variational and EnKF methods and to overcome their respective shortcomings, hybrid ensemble and variational DA methods were proposed by Barker (1999), Hamill and Snyder (2000), and Lorenc (2003). In these hybrid methods, the flow-dependent background error covariance estimated from the ensemble members and the static background error covariance that is commonly used in a variational framework are combined to form a hybrid covariance, which is built into the cost function. For large-scale DA, hybrid methods have been successfully demonstrated by Hamill and Snyder (2000), Buehner (2005), Zupanski (2005), and X. Wang et al. (2008a,b, 2013). Furthermore, Barker et al. (2012), Li et al. (2012), and Zhang et al. (2013) recently reported on the capability of a hybrid system for mesoscale weather events. Several global operational NWP centers have also adopted this method, as reported in Buehner et al. (2010a,b), wherein forecast improvements were found where observations are sparse, whereas a hybrid method within the Met Office unified global NWP system led to only very modest forecast improvements (Clayton et al. 2013). Liu et al. (2008, 2009) proposed a

different hybrid ensemble and variational formulation in which the four-dimensional background error covariances were estimated from an ensemble of forecasts and used in a variational framework without using the tangent-linear or adjoint versions of the forecast model. This method is attractive because of its easy implementation in operational environments (Clayton et al. 2013).

Another type of hybrid method for calculating background error covariance statistics that holds good promise is an ensemble of DAs (Kucukkaraca and Fisher 2006; Berre et al. 2007; Bonavita et al. 2012). In this method, an ensemble of variational analyses is executed, with each analysis created from a perturbed initial condition with perturbed observations. This approach unifies the ensemble forecast and DA systems, while allowing existing variational approaches to be used with little modification. It has been applied using an ensemble of 4DVAR by Meteo France (Kucukkaraca and Fisher 2006; Berre et al. 2007) and ECMWF (Bonavita et al. 2012). In both centers, a 4DVAR system is being used, with tangent-linear and adjoint models such that the observational information is propagated throughout the data-assimilation window in a dynamically consistent manner. One key drawback of using an ensemble of 4DVAR is the computational cost involved, which limits the attainable ensemble size and therefore requires special filter techniques to smooth the noisy ensemble variance (Berre et al. 2007; Bonavita et al. 2012).

Inspired by the success of hybrid strategies using flow-dependent ensemble information in variational methods, Gao et al. (2013b) and Gao and Stensrud (2014) demonstrated the potential of a hybrid 3DVAR and EnKF method for convective-scale DA. Following Bowler et al. (2013), this approach was called 3DEnVAR. The algorithm uses the extended control variable approach to combine the static and ensemble-derived flow-dependent background error covariance to form a hybrid covariance. Results with simulated radar observations of a supercell storm indicated the hybrid method provides better analyses for small ensembles than the 3DVAR, EnKF, and 3DEnVAR with pure ensemble covariance. For relatively large ensemble sizes (50–100), the performance of the hybrid method is close to that of EnKF, and both are significantly better than that of the 3DVAR. Sensitivity experiments indicate that the best results occur when the number of the augmented control variables is a function of three spatial dimensions and ensemble members and is the same for all analysis variables (Gao and Stensrud 2014). In the above study, the EnKF method was involved. Because radar data are usually in high density, the use of EnKF method in the

hybrid approach is also very computationally expensive, especially for convective-scale NWP.

In this study, we adopt the ensemble of DAs (EDA) concept discussed above and used by Meteo France and ECMWF (Berre et al. 2007; Bonavita et al. 2012) for convective-scale data DA but use the extended control variable method to introduce ensemble covariance into the variational system. This EDA approach would be very expensive if the inner core DA scheme was 4DVAR. Here we use 3DVAR, which is computationally much more efficient. The approach is labeled En3DA, as it consists of an ensemble of 3DVAR analyses. The advantage of this method is that it can produce multivariant flow-dependent background error covariances, which are particularly needed in convective-scale radar DA because of the limited number of observation types (i.e., radar only provides radial velocity, reflectivity, and various quantities derived from dual polarization of the radar signal, none of which are prognostic variable in most NWP models).

In section 2, we briefly introduce the En3DA methods, while section 3 describes the DA experiment design. In section 4, sensitivity experiments and quantitative performance are assessed in section 5. We conclude in section 6 with a summary and outlook for future work.

## 2. Description of DA method

In the following, we briefly describe the En3DA method used in this study. Suppose we have ensemble forecasts from  $K$  ensemble members, which can be denoted as  $\mathbf{x}_1^b, \mathbf{x}_2^b, \dots, \mathbf{x}_k^b$ ; it is convenient to denote a matrix  $\mathbf{E}$ , the columns of which are defined by normalized differences between the ensemble-member forecasts and the ensemble mean:

$$\mathbf{E} = (\mathbf{x}_1^b - \bar{\mathbf{x}}^b, \mathbf{x}_2^b - \bar{\mathbf{x}}^b, \dots, \mathbf{x}_k^b - \bar{\mathbf{x}}^b) / \sqrt{K-1}. \tag{1}$$

Then the ensemble covariance  $\mathbf{P}_e$  is given by

$$\mathbf{P}_e = \mathbf{E}\mathbf{E}^T. \tag{2}$$

The rank of the above constructed ensemble covariance is ensemble size  $K$ . Because of the limitation of computer resources,  $K$  is usually much smaller than the number of degrees of freedom in the NWP model, and this causes a low-rank problem and associated sampling error. To solve the above problem, Houtekamer and Mitchell (2001) proposed using the Schur product defined in Gaspari and Cohn (1999) by

$$\mathbf{B}_e = \mathbf{C} \circ \mathbf{P}_e^T. \tag{3}$$

Here,  $\mathbf{C}$  is a localization covariance, or correlation matrix, and  $\circ$  stands for the element-by-element product of two matrices with the same dimension. The purpose of using matrix  $\mathbf{C}$  is to filter out the small ensemble correlations that may be dominated by sampling noise associated with remote observations while keeping the robust correlations closer to observations relatively unaffected. By doing this, the conditioning of original ensemble covariance matrix  $\mathbf{P}_e$  is greatly improved. The procedure of localization is fully discussed in Lorenc (2003), Buehner (2005), and Wang et al. (2007) and is not repeated here. There are several ways to conduct covariance localization (Bishop et al. 2011), with the most often used being matrix  $\mathbf{C}$  as a compactly supported fifth-order piecewise rational function given by Gaspari and Cohn (1999). The effect of this localization function is modeled by a recursive filter (Purser et al. 2003a,b) for simplicity, which is suggested by Wang et al. (2008a).

The cost function,  $J_k$ , where  $k = 1, 2, \dots, K$  used in the En3DA is defined as the sum of the background and observational terms plus a penalty or equation constraint term:

$$J_k = \frac{1}{2}(\mathbf{x}_k - \mathbf{x}_k^b)^T \mathbf{B}^{-1}(\mathbf{x}_k - \mathbf{x}_k^b) + \frac{1}{2}[\mathbf{H}(\mathbf{x}_k) - \mathbf{y}_k^o]^T \mathbf{R}^{-1}[\mathbf{H}(\mathbf{x}_k) - \mathbf{y}_k^o] + J_c(\mathbf{x}_k). \quad (4)$$

Here,  $\mathbf{x}_k$  are the analysis vectors and  $\mathbf{x}_k^b$  are the background state vectors from the ensemble forecasts defined in (1),  $\mathbf{H}(\mathbf{x})$  is the observation operator, and  $\mathbf{y}_k^o$  is the observation vector for ensemble member  $k$ . Here,  $\mathbf{y}_k^o$  can be the same vector for every ensemble member or can be different for each ensemble member by applying

$$J_k = \frac{1}{2}\mathbf{v}_k^T \mathbf{v}_k + \frac{1}{2}[\mathbf{H}(\mathbf{x}_k^b + \mathbf{B}_e^{1/2}\mathbf{v}_k) - \mathbf{y}_k^o]^T \mathbf{R}^{-1}[\mathbf{H}(\mathbf{x}_k^b + \mathbf{B}_e^{1/2}\mathbf{v}_k) - \mathbf{y}_k^o] + J_c(\mathbf{v}_k). \quad (5)$$

In the standard 3DVAR scheme, the square root of matrix background error covariance  $\mathbf{B}$  is static and usually significantly simplified as, for example, a recursive filter to model the covariance structure (Purser et al. 2003a,b). In this study, the matrix  $\mathbf{B}_e$  [defined in (3)] is derived from an ensemble of forecasts so each analysis with (5) can also be called a 3DEnVAR scheme. For computational efficiency, we also use the recursive filter to localize the ensemble covariance in model space (Wang et al. 2008a). By using new control variables  $\mathbf{v}$ , the minimization procedure is preconditioned by square root of the flow-dependent background error

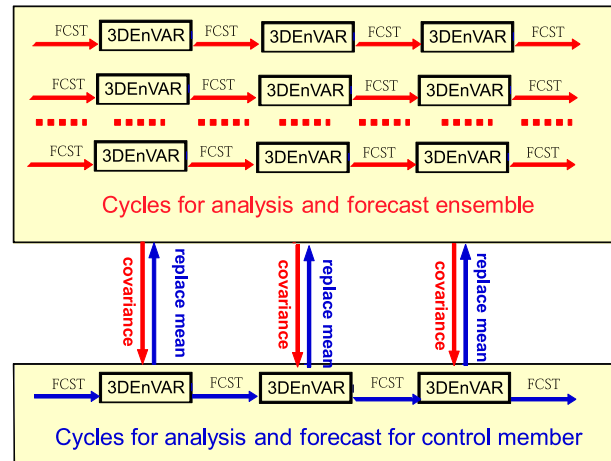


FIG. 1. Illustration of cycle used in an ensemble of 3DEnVAR analysis scheme.

random perturbations to the original observations. The term  $J_c$  in (4) includes any penalty or dynamic equation constraint terms that may be added to serve the important role of correlating the desired analysis variables. The mass continuity equation is imposed as a weak constraint in (4) and many previous applications (Gao et al. 1999, 2004), and details regarding this constraint are discussed in the experiment design and results sections. Matrix  $\mathbf{R}$  is the observation error covariance matrix. To effectively precondition the minimization problem, we follow Derber and Rosati (1989) and Courtier (1997) and define an alternative control variable  $\mathbf{v}$  such that analysis increment  $\Delta\mathbf{x}_k = \mathbf{B}_e^{1/2}\mathbf{v}_k = (\mathbf{x}_k - \mathbf{x}_k^b)$ , which allows the cost function to be changed into a preconditioned incremental form such that

covariance, denoted by  $\mathbf{B}_e^{1/2}$ . The forecast ensemble-derived flow-dependent  $\mathbf{B}_e$ , in particular the cross covariances between different model variables, are nonzero and thus should be more useful than the simple static covariance (wherein the cross covariances are zero) implemented in Gao and Stensrud (2012).

In addition, an extra model integration for the length of the analysis cycle is needed to produce a control forecast and analysis cycle. An ensemble of the 3DEnVAR analyses is performed by minimizing the cost function (5)  $K$  separate times to update the analysis increment for each ensemble member (which starts from a different initial condition; see Fig. 1). Each 3DEnVAR

analysis uses the ensemble covariance derived from other ensemble forecasts except for the forecast used as background field for itself, thereby avoiding the potential underestimation of the variance of the background errors (Houtekamer and Mitchell 1998; Hamill and Snyder 2000). For example, the member-1 3DnVAR analysis uses ensemble covariance derived from ensemble members 2– $K$ ; member-2 3DnVAR uses ensemble covariance derived from members 1 and 3– $K$ , and finally the control member 3DnVAR analysis uses covariance derived from ensemble members 1– $K$ . In this way, the ensemble information is used in every 3DnVAR analysis. Each 3DnVAR analysis in the En3DA scheme is then recentered using the control analysis. The idea of the dual-resolution concept [Gao and Xue (2008); not used in this study] can be easily implemented as well. After the initial conditions for the ensemble and one control forecast are obtained, the ensemble forecasts are launched. The above steps are repeated for each DA cycle. However, early testing suggests that the ensemble spread may be smaller than desired, so a postprocessing step is applied to the analysis ensemble according to

$$\mathbf{x}_k^a = \mathbf{x}_c^a + \gamma(\mathbf{x}_k^a - \bar{\mathbf{x}}^a) + (1 - \gamma)(\mathbf{x}_k^b - \bar{\mathbf{x}}^a), \quad (6)$$

where the first term denotes the analysis for the control member, the second term denotes a perturbation from the analysis ensemble mean, and the third term represents a perturbation from background ensemble mean. Thus, the ensemble is recentered around the control member, but the analysis perturbations are mixed with the forecast perturbations. We choose  $\gamma = 0.5$ , which is similar to the relaxation-to-prior method proposed by Zhang et al. (2004), in which covariance inflation is achieved by mixing forecast and analysis perturbations.

In the application of this En3DA scheme, both radar reflectivity and radial velocity data are assimilated similar to Gao et al. (2013b) and Gao and Stensrud (2014). The reflectivity forward operator is adopted from Gao and Stensrud (2012), which is briefly discussed in next section. The analysis variables  $\mathbf{x}$  contain the three wind components  $u$ ,  $v$ , and  $w$ ; potential temperature  $\theta$ ; pressure  $p$ ; water vapor mixing ratio  $q_w$ ; and the hydrometeor-related model variables, including the mixing ratios for cloud water  $q_c$ , cloud ice  $q_i$ , rainwater  $q_r$ , snow  $q_s$ , and hail  $q_h$ , the latter three of which are added to the analysis vector to assimilate reflectivity directly in a variational framework (Gao and Stensrud 2012).

This En3DA scheme produces an analysis that is similar to an EnKF scheme, as the En3DA scheme is

essentially a variational formulation with ensemble-derived covariance. One advantage of this method over the EnKF method is that weak constraints such as the mass continuity equation can be incorporated in the cost function so that a balanced analysis among different model variables may be achieved. The En3DA method also is computationally more efficient than the EnKF method. Although the control variables are defined differently from the analysis variables, the form of the cost function has not changed much from that found in a standard 3DVAR so that codes from an existing 3DVAR system can readily be utilized.

### 3. Model and experimental design

#### a. Prediction model and truth simulation for OSSEs

The En3DA algorithm described above is tested with simulated data from a classic supercell storm event from 20 May 1977 near Del City, Oklahoma (Ray et al. 1981). The ARPS model is used in a 3D cloud model mode, and the prognostic variables are the same as the analysis variables described above. The single-moment, three-category ice scheme of Lin et al. (1983) is used to describe the microphysical processes. More details on ARPS can be found in Xue et al. (2000, 2001, 2003).

The model domain is chosen as  $57 \times 57 \times 16 \text{ km}^3$ . The horizontal grid spacing is 1 km, and the mean vertical grid spacing is 500 m without stretching. The truth simulation run is initialized from a horizontally homogeneous background environment defined by a modified real sounding taken at Norman, Oklahoma, plus an ellipsoidal thermal bubble with potential temperature perturbation of 4 K located at  $x = 48 \text{ km}$ ,  $y = 16 \text{ km}$ , and  $z = 1.5 \text{ km}$ , with radii of 10 km in  $x$  and  $y$  and 1.5 km in the  $z$  direction. Open lateral boundary conditions are used. The length of the truth simulation is 90 min, and this is long enough to cover the DA period. To keep the primary storm cell near the center of model domain, a constant wind with  $u = 3 \text{ m s}^{-1}$  and  $v = 14 \text{ m s}^{-1}$  is subtracted from the observed sounding. Similar to Xue et al. (2001), the initial convective cell develops over the first 30 min, with cloud starting to form at about 10 min and rainwater appearing at about 15 min. Ice-phase fields appear at about 20 min into the run. The strength of the cell reaches peak intensity near 30 min and then decreases between 30 and 60 min. The cell splits at around 55 min, a behavior indicative of a classic supercell thunderstorm. The right-moving cell (relative to the storm motion vector, which is toward north-northeast) becomes stronger after this point, with its tilted reflectivity core and warm center collocated with a strong mesocyclone in the middle levels (from 5 to 8 km above the ground) and a strong cold pool near the surface at

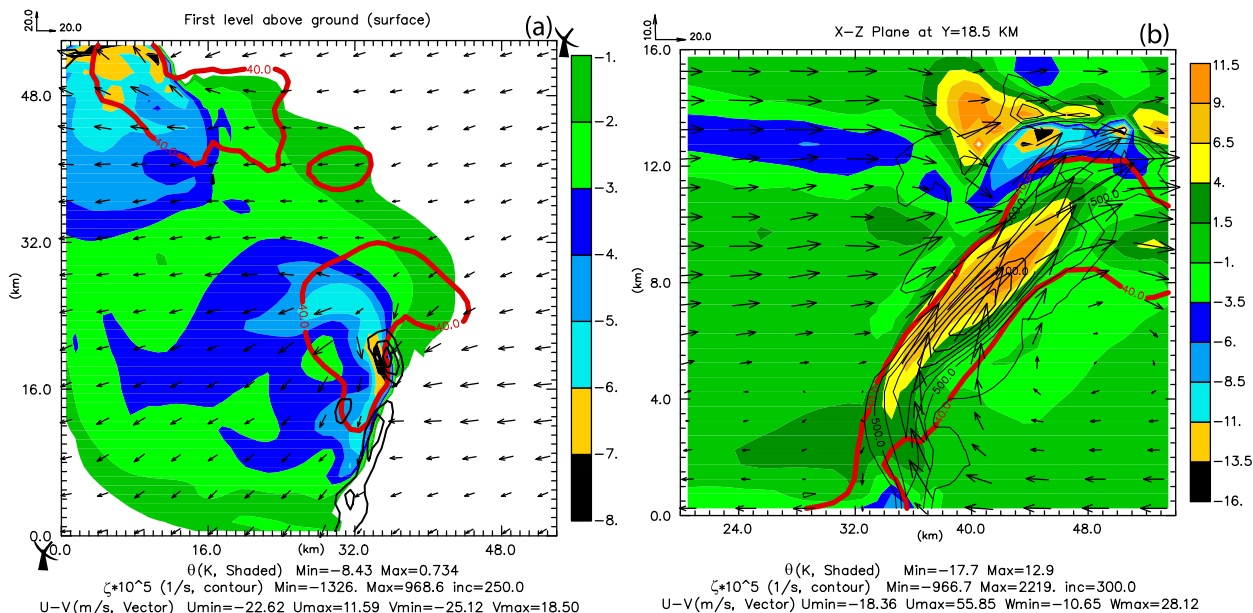


FIG. 2. ARPS model-simulated wind vectors, vertical vorticity  $\zeta$  (black contours), and perturbation potential temperature  $\theta$  (shaded) fields of the 20 May 1977 supercell storm at 90 min as reference truth. (a) Horizontal cross section at first level above ground; (b) vertical cross section at  $y = 18.5$  km in (a). Red solid lines are for reflectivity fields at 40 dBZ. The two radar locations are indicated at the bottom-left and top-right corners.

90 min (Fig. 2). A similar truth simulation was also used in Gao et al. (1999, 2004, 2013b), Tong and Xue (2005), and Gao and Stensrud (2012).

### b. Simulation of radar observations

The simulated radial velocity observations are derived from the truth simulation wind field defined on the model grids, as if one radar was positioned in the southwest corner of the domain and another located in the northeast corner. This radar network design leads to some poor cross-beam angles near the ground as the storm is maintained near the domain center. However, there is very strong vertical shear in terms of both direction and amplitude in the storm environment. Consequently, the radar-storm geometry in middle and upper levels is more favorable (good cross-beam angles). This could cast an overly positive light on expected analysis improvements. However, it is not uncommon for storms to occur in locations with poor cross-beam angles within the current operational WSR-88D network. Thus, we believe that the radar-storm geometry used in the experiments is reasonable for these early evaluations of the method.

The three wind components  $u$ ,  $v$ , and  $w$  are projected to the radial directions to obtain the simulated Doppler radar radial velocity data using the azimuth of the radial direction and the local slope of the radar beam following a curving ray path:

$$v_r = \frac{dh}{dr} w + \frac{ds}{dr} (u \sin \varnothing + v \cos \varnothing), \quad (7)$$

where  $v_r$  is the projected radial velocity,  $r$  is the slant range (ray path distance),  $h$  is the height above the curving surface of Earth,  $s$  is the distance along Earth's surface, and  $\varnothing$  is the radar azimuth angle. To model WSR-88Ds in precipitation mode, 14 different elevations angles are used that reproduce the operational WSR-88D scanning strategy (Maddox et al. 2002).

Differentiating the equation for the height of the radar beam from the four-thirds-Earth ray-path equations (from, e.g., Doviak and Zrníć 1993), one can derive the local slope of the ray path:

$$\frac{dh}{dr} = \left( r + \frac{4}{3} a \sin \theta_e \right) \left[ r^2 + \left( \frac{4}{3} a \right)^2 + \frac{8}{3} a r \sin \theta_e \right]^{-1/2}, \quad (8)$$

where  $a$  is Earth's radius, and  $\theta_e$  is the radar elevation angle. From the grid point's location with respect to the radar and the four-thirds-Earth model for the ray path, one can obtain the needed elevation angle and slant range:

$$\theta_e = \tan^{-1} \left( \frac{H \cos S - k_e a}{H \sin S} \right) \quad \text{and} \quad (9)$$

$$r = \frac{H \sin S}{\cos \theta_e}, \quad (10)$$

where  $H = (4/3)a + (z - z_{\text{radar}})$ ,  $s = 3s/4a$ , and  $z_{\text{radar}}$  is the height of the radar. Ge et al. (2010) tested the effects of beam broadening and Earth curvature in the radar radial velocity forward operator within radar DA and found that the former effect can be generally overlooked while the latter should be considered. Thus, in this study the effect of beam broadening is neglected, but the effect of Earth curvature is included.

The simulated reflectivity observations are calculated based on Smith et al. (1975) and Ferrier (1994) for the Lin et al. (1983) microphysics scheme. The forward model for equivalent radar reflectivity factor is obtained by collecting the contributions from the three precipitating hydrometeor mixing ratios—rain, snow, and hail—using the following formulation:

$$Z_e = Z(q_r) + Z(q_s) + Z(q_h) \quad \text{and} \quad (11)$$

$$Z_{\text{dB}} = 10 \log_{10} Z_e. \quad (12)$$

The assimilation of reflectivity observations is complicated because the reflectivity factor is a nonlinear function of all three hydrometeor variables (rainwater, snow, and hail). This leads to the DA solution being underdetermined. Thus, it is possible to obtain a non-zero snow mixing ratio in the low levels of the model where only rainwater is expected because of the very warm temperatures at these levels. To prevent this, the forward reflectivity operator from Gao and Stensrud (2012), which uses the background temperature from an NWP model for hydrometer classification, is used in this study.

Random errors are added to the simulated observations at each observation location. For reflectivity, random errors are drawn from a normal distribution with a mean of 0 dBZ and a standard deviation of 4 dBZ. For radial velocity  $v_r$ , random errors are drawn from a normal distribution with a mean of 0  $\text{m s}^{-1}$  and a standard deviation of 1  $\text{m s}^{-1}$  (or 5  $\text{m s}^{-1}$  in some sensitivity experiments). For most experiments, this same group of perturbed reflectivity and radial velocity observations are used for every ensemble member of 3DnVAR analysis. Since  $v_r$  is sampled directly from the simulated model velocity fields, hydrometeor sedimentation is not involved. In all of the experiments, radial velocities are assimilated where reflectivities are greater than 15 dBZ and model height levels are greater than 1.5 km, or where reflectivities are greater than 25 dBZ and model height levels are less than 1.5 km. These criteria were set to reduce the impact of ground clutter and other nonweather echoes in the old 3DVAR program (Gao et al. 2004) for real-time applications and also are adopted here.

### c. Design of assimilation experiments

Similar to Gao and Stensrud (2014), we start the En3DA experiments at 30 min of the model integration time when the storm cell is becoming well developed. Also based on the experiments performed in Gao and Stensrud (2014), the ensemble size is set to 50 in this study. To initialize the ensemble members, random noise is added to the initially horizontally homogeneous first guess throughout the model domain. The random noise is sampled from Gaussian distributions with zero mean and standard deviations of 5  $\text{m s}^{-1}$  for  $u$ ,  $v$ , and  $w$  and 3 K for potential temperature. A 2D five-point smoother is applied to the resultant fields, similar to a method used by Zupanski et al. (2006). The initial perturbation variances are somewhat larger than those used in Tong and Xue (2005), but the standard deviation of the final perturbations is not necessarily larger because of the smoothing. Other model variables, including the microphysical variables, are not perturbed at the initial time. The radial velocity and reflectivity observations are calculated and assimilated using a 5-min cycle in all DA experiments with the first analysis performed at 30 min. The localization scale for the recursive filter is 4 km horizontally and 1 km vertically. One baseline experiment and several sensitivity experiments are performed in this study.

For the baseline analysis and forecast experiment, the Lin microphysics scheme (Lin et al. 1983) is used in the ensemble forecasts, and the mass continuity equation is used as a weak constraint. Radial velocity and reflectivity are assimilated using a threshold reflectivity value of 15 dBZ (other threshold values are chosen for some sensitivity experiments). While the mass continuity equation constraint is critical for analyzing vertical velocities in 3DVAR schemes in earlier studies (Gao et al. 1999, 2004; Hu et al. 2006), its impact for this ensemble-related DA scheme is uncertain and thus is studied here.

The first set of sensitivity experiments is performed to test the usefulness of the mass continuity constraint by not including it in the minimization of the cost function and using random radial velocity observation error amplitudes of both 1 and 5  $\text{m s}^{-1}$ . In reality, radial velocity observations may contain large errors from other sources, particularly because of bias errors related to velocity aliasing, ground clutter, and anomalous propagation (Doviak and Zrnić 1993). In real data simulations, these problems often are addressed during the radar quality-control step before the DA, although automatic outlier rejection and velocity dealiasing developed to operate during DA have proven to be simple and effective for convective-scale radar DA for the

NCAR WRF Model ensemble data assimilation system (Yussouf et al. 2013). The possible impact of bad data getting through quality control and contaminating the analysis has not been thoroughly examined.

The second set of experiments is performed to test the sensitivity of assimilating radar observations to changes in microphysics schemes and their combinations used in the ensemble analysis and forecasts. In the baseline experiment, only the Lin microphysics scheme (Lin et al. 1993) is used. For the sensitivity experiments, three additional experiments with different microphysics schemes are performed. One of the experiments uses the so-called three-class ice microphysics (3-ICE) scheme (Gilmore et al. 2004), which is a single-moment scheme similar to the Lin scheme. Another experiment uses the two-moment version of the Milbrandt and Yau (2005) microphysics scheme. In this scheme, both the mass mixing ratios and their corresponding total number concentrations are predicted variables, which makes this scheme very different from the Lin and 3-ICE schemes. In the final microphysics sensitivity experiment, we use a mixture of these three microphysics schemes: that is, among the 50 ensemble members, 16 use the Milbrandt–Yau scheme, another 16 use the Lin scheme, and the remaining members use the 3-ICE scheme. The analysis and forecast cycle for the single control member uses the Milbrandt–Yau scheme.

The third set of sensitivity experiments is performed with different threshold values of reflectivity observations. As indicated in (11) and (12) [also in Gao and Stensrud (2014)], the forward operator for reflectivity is nonlinear, and it is difficult to assimilate highly nonlinear observations into an NWP model. Past experience indicates that DA analysis results are sensitive to reflectivity observations with low values of reflectivity. Particularly problematic is the fact that spurious storm cells often develop when low values of reflectivity are assimilated. Four more experiments are performed to test the threshold reflectivity value, with three of them assimilating reflectivity above the threshold values 5, 15, and 35 dBZ. For reflectivity below these threshold values, they are treated as 0 dBZ and also assimilated to suppress spurious convections.

The final sensitivity experiment tests the performance of the En3DA when the radial velocity observations are perturbed differently but with the same mean and standard deviation for each ensemble member of the 3DEnVAR analysis. The purpose of this experiment is to find out whether it is necessary to perturb the observations for each ensemble member to benefit the En3DA method for convective-scale applications.

For comparison purposes, all DA experiments are performed with 12 DA cycles, where each cycle has a

5-min analysis–prediction interval. The total assimilation period is 60 min, and the first analysis occurs at 30 min.

## 4. Results

### a. The baseline experiment

The baseline experiment serves as a benchmark for all of the following sensitivity experiments. To examine the quality of the DA results more closely, we show in Figs. 3a and 3b sample plots for the control member analysis at the end of the DA cycle. Comparisons with the true fields shown in Fig. 2 indicate that most storm features, such as the low-level convergence zone, strong tilted updraft core, midlevel mesocyclone, low-level cold pool, and midlevel warm core, are well recovered. While the strength of the cold pool is a little bit weak (the minimum perturbation potential temperature is  $-6.9\text{K}$  compared with  $-8.4\text{K}$  in the truth simulation), the thermodynamic structures at the middle and upper levels are well analyzed (Fig. 3b). The reflectivity field indicates that the general precipitation patterns look very similar near the surface (Fig. 3a vs Fig. 2a). The vertical extension of the reflectivity core matches the truth simulation very well except for some small bias near the 10-km level. The rms errors of the  $u$  component of horizontal wind field, vertical velocity  $w$ , perturbation pressure  $p$ , and water vapor mixing ratio  $q_v$  for the control experiment are shown in red curves in Fig. 4. Generally the errors decrease gradually, starting from the first analysis, and reduce by 80% at the end of DA cycles for the majority of the model variables. The important features of this supercell storm are well analyzed in this control experiment.

In the baseline experiment, an extra analysis and forecast cycle member is used, and each ensemble analysis is recentered on the control member analysis. Actually, there is another option to recenter the analysis with the ensemble mean of 3DEnVAR analyses. The evolution of rms errors with ensemble mean versus the control member analysis in the baseline experiment is shown in Fig. 5. The performances are quite similar for most of the model variables during the 1-h data assimilation period. Toward the end of DA cycle, however, the baseline experiment in which the ensemble is recentered on the control member analysis gives slightly better results (Fig. 5). This result suggests the potential value of a dual-resolution system in which a single very high-resolution control member and a relatively low-resolution ensemble are performed simultaneously. Both ECMWF and NCEP ensemble systems currently have this

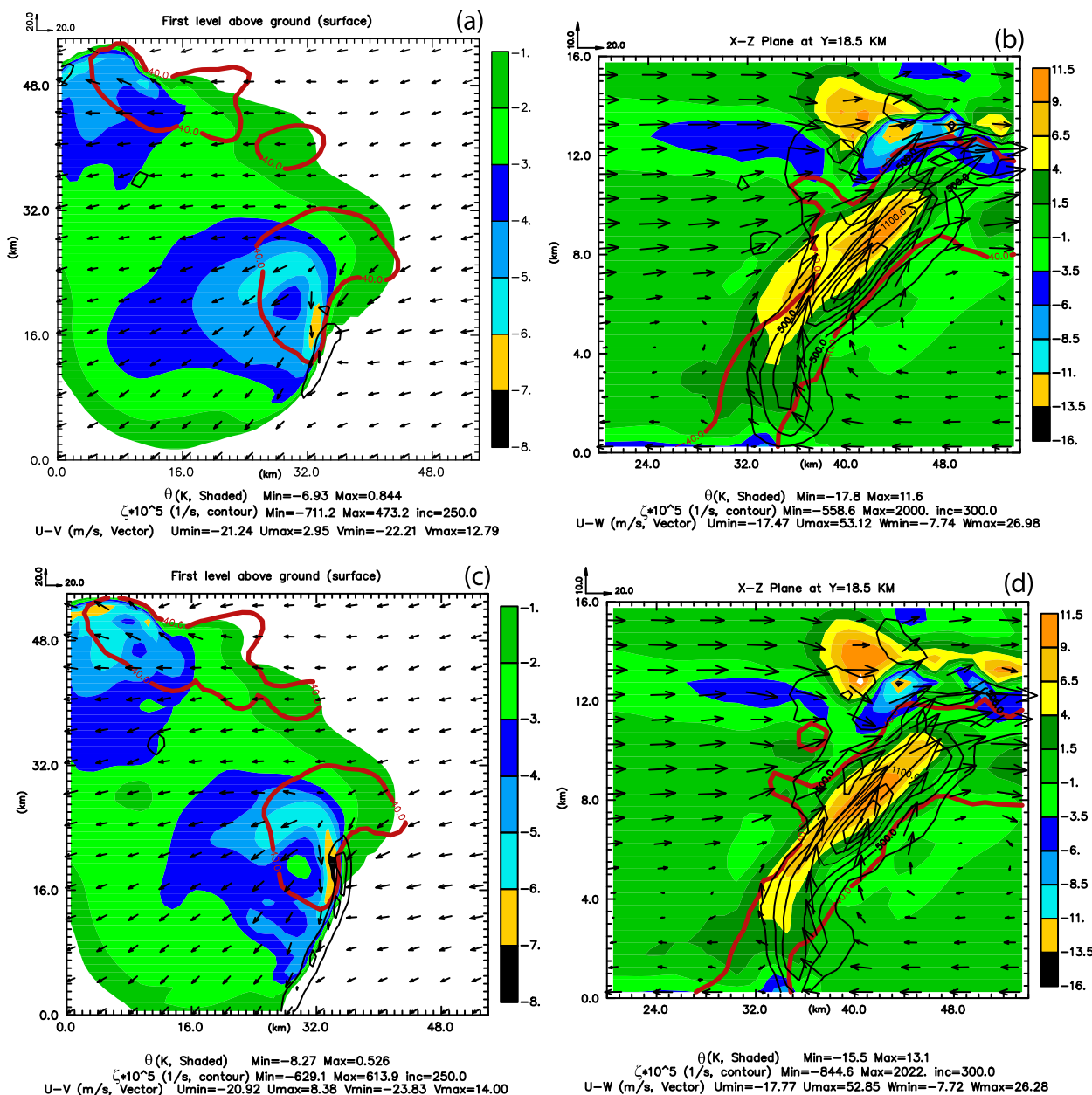


FIG. 3. As in Fig. 2, but for 3DEnVAR analysis with a radial velocity error of  $1 \text{ m s}^{-1}$ . (a),(b) The baseline experiment with mass continuity constraint; (c),(d) the experiment without mass continuity constraint. Red solid lines are for reflectivity fields at 40 dBZ.

kind of dual-resolution structure (Du 2004; Bonavita et al. 2012).

*b. Sensitivity experiments with mass continuity equation as a weak constraint*

An earlier study by Gao et al. (1999) suggests that, to obtain a reasonable three-dimensional wind field, the mass continuity equation needs to be used as a weak constraint instead of a strong constraint in 3DVAR. Within this En3DA method, including a mass continuity

equation may benefit not only the wind field analysis but also the analyses of the other model variables, such as pressure and moisture variables, via the cross covariances in the error covariance matrix. Several sensitivity experiments are performed in this section to explore this question. Thus, the first sensitivity experiment is exactly the same as the baseline, except that the mass continuity constraint is neglected.

The analysis at the end of DA cycles without using mass continuity constraint looks better than the baseline,

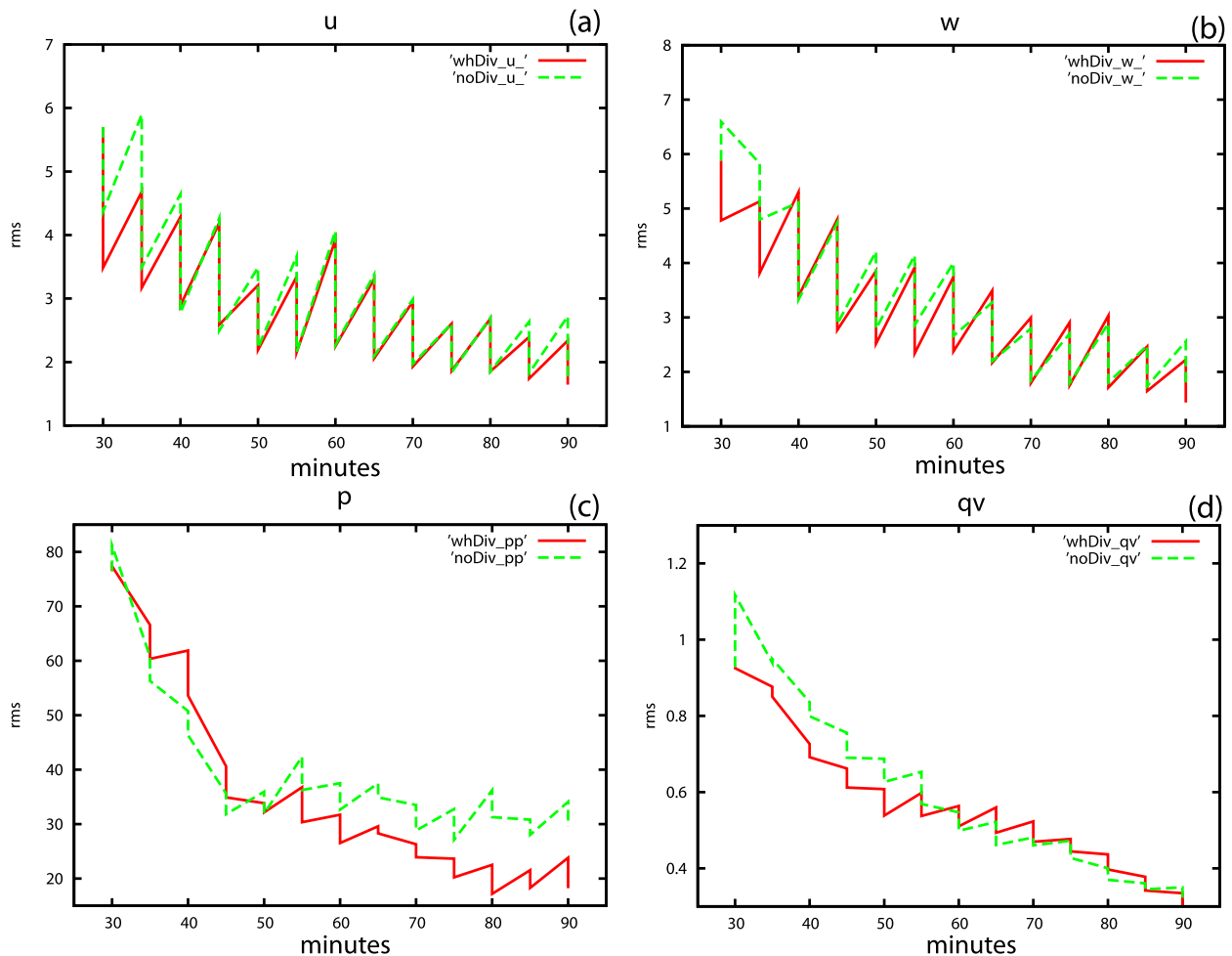


FIG. 4. The rms errors of the analysis and forecast for radial velocity observations contain errors of  $1 \text{ m s}^{-1}$ . (a) Horizontal wind component  $u$  ( $\text{m s}^{-1}$ ); (b) vertical velocity  $w$  ( $\text{m s}^{-1}$ ); (c) perturbation pressure  $p$  (hpa); and (d) water vapor mixing ratio  $q_v$  ( $\text{g kg}^{-1}$ ). Red and green correspond to the experiments with and without mass continuity constraint, respectively.

especially the representation of the cold pool, where the minimum perturbation potential temperature is  $-8.27 \text{ K}$  (Fig. 3c), closer to the reference true value, which is  $-8.43 \text{ K}$  (Fig. 2a). The leading edge of the gust front (indicated by a stripe of black vorticity contours) also is sharper. By only viewing these quantities, it looks like the analysis improves when no mass continuity equation is used. But if we compare the reflectivity pattern (represented by the 40-dBZ contour line), the three precipitation areas are combined into two areas. Comparing Fig. 3d with Fig. 3b, we see that the analysis without the mass continuity equation contains more small noise even though the analysis generally looks better. Figure 4 shows that the rms errors are larger when no mass continuity constraint is used during the first two analysis cycles, especially for the  $u$  component of horizontal wind, vertical velocity  $w$ , and water vapor mixing ratio  $q_v$ . The final rms errors after the 60-min assimilation period with (red

curves in Fig. 4) and without (green curves) the mass continuity equation are quite similar, except for pressure  $p$  (Fig. 4c), for which rms errors with the mass continuity constraint are smaller. So a quick glance appears to indicate that the role of mass continuity constraint has mixed impact on the analysis results in this case.

A closer examination suggests that the analysis looks more balanced when using the mass continuity constraint. For an example, Fig. 6 shows reflectivity, wind vectors, and water vapor mixing ratios in a vertical cross section at  $y = 18.5 \text{ km}$  after two data assimilation cycles. By comparing the analyses to the truth simulation, we can see the changes produced by imposing the mass continuity constraint. For reflectivity, the analysis with mass continuity shows a precipitation pattern that is smooth and has two descending zones of higher reflectivity starting from the anvil region, as also seen in the truth simulation (Fig. 6a vs Fig. 6b). This feature

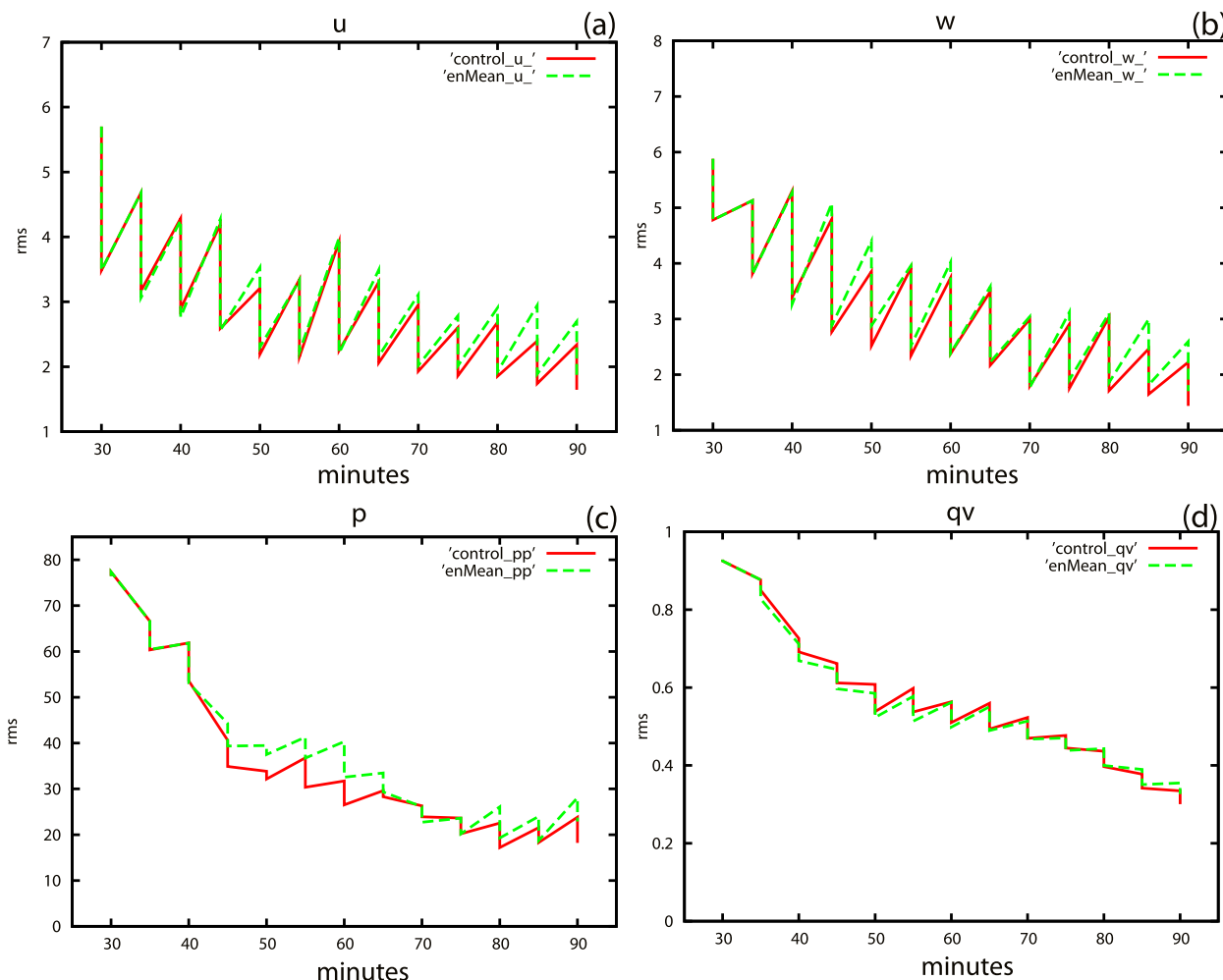


FIG. 5. As in Fig. 4, but the red curve corresponds to the baseline experiment. The green curve corresponds to the experiment with ensemble mean of 3DENVAR analyses.

does not appear in the analysis without mass continuity; this analysis also shows more biased precipitation in the low portion of the anvil area (Fig. 6a vs Fig. 6c). Though it is hard to see from wind vectors (Figs. 6d,e,f), the rms errors for winds indicate that the analysis with mass continuity is slightly better. For water vapor mixing ratio, the analysis with mass continuity constraint is clearly much closer to the truth simulation (Figs. 6d,e,f). To further demonstrate the benefit of the mass continuity constraint, Fig. 7 shows the 1-h forecast initialized from the ensemble mean generated with and without mass continuity. In general, the forecast for nearly all model variables is better for the experiment with mass continuity than without mass continuity, as indicated by lower rms errors throughout most of the 1-h period.

In the above experiments, we have assumed that the radial velocity observations have random errors with a standard deviation of  $1 \text{ m s}^{-1}$ . In real cases, these

errors can be larger. So in the following two sensitivity experiments (one with mass continuity constraint and the other without it), we assume that the radial velocity observations have random errors with a standard deviation of  $5 \text{ m s}^{-1}$ , so the amplitude of errors for radial velocity are increased by a factor of 5. The resulting rms errors for the experiment with the mass continuity constraint do not increase very much (red curves in Fig. 8 vs those in Fig. 4). In contrast, the rms errors for the experiment without the mass continuity constraint increase by a large margin (green curves in Fig. 8), though these errors are still generally reduced with the DA cycles moving forward. The rms errors for the experiment without the constraint at the beginning of the DA cycles are especially high for vertical velocity  $w$  and water vapor mixing ratio  $q_v$ . At the end of the DA period, rms errors for all selected variables are larger for the experiment without the mass continuity constraint.

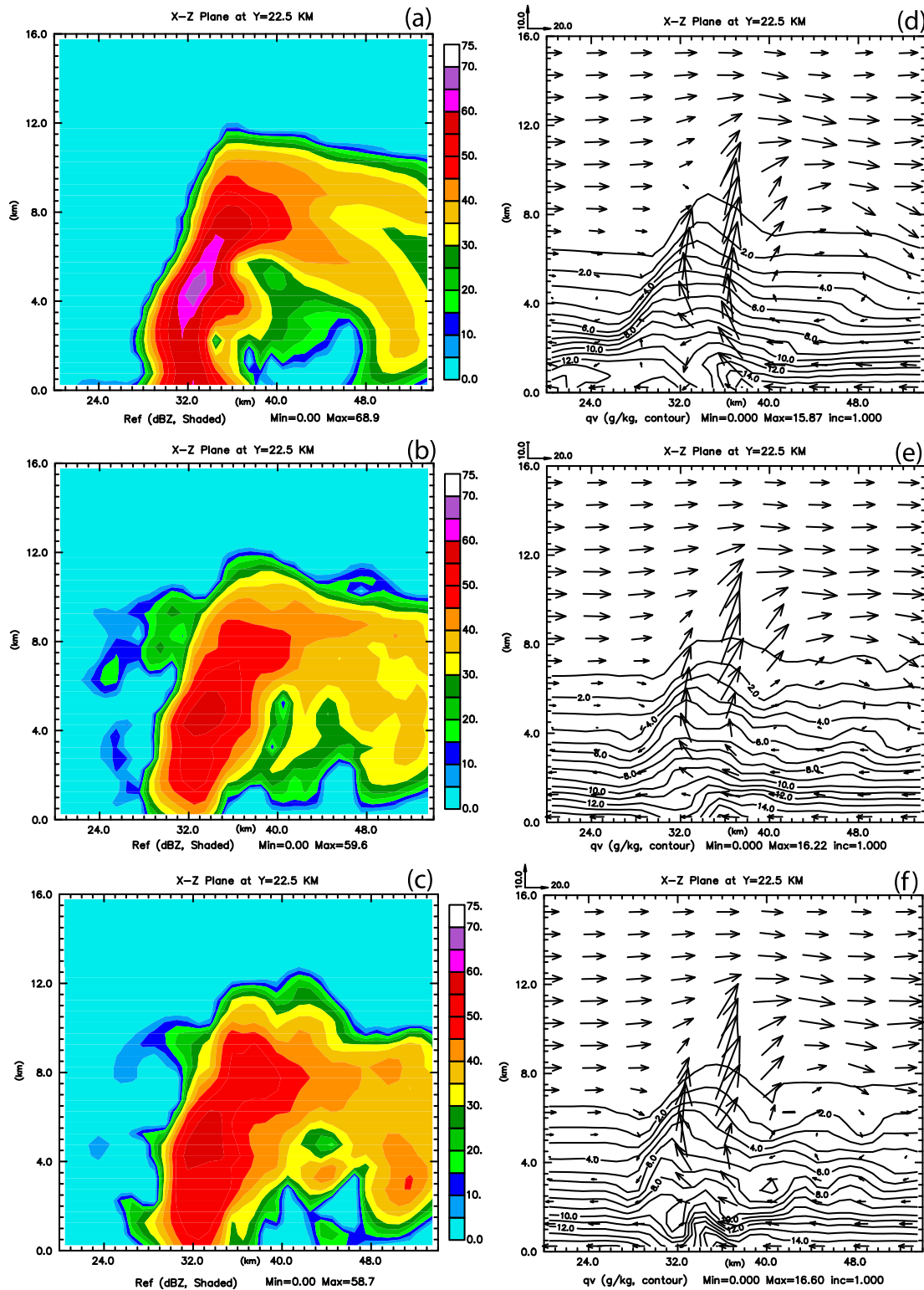


FIG. 6. (a)–(c) Reflectivity and (d)–(f) wind vectors and water vapor mixing ratio (contours) in a vertical cross section at  $y = 18.5$  km after only two assimilation cycles for radial velocity observations containing errors of  $1 \text{ m s}^{-1}$  for (a), (d) the reference truth; (b), (e) the experiment with mass continuity constraint; and (c), (f) the experiment without mass continuity constraint.

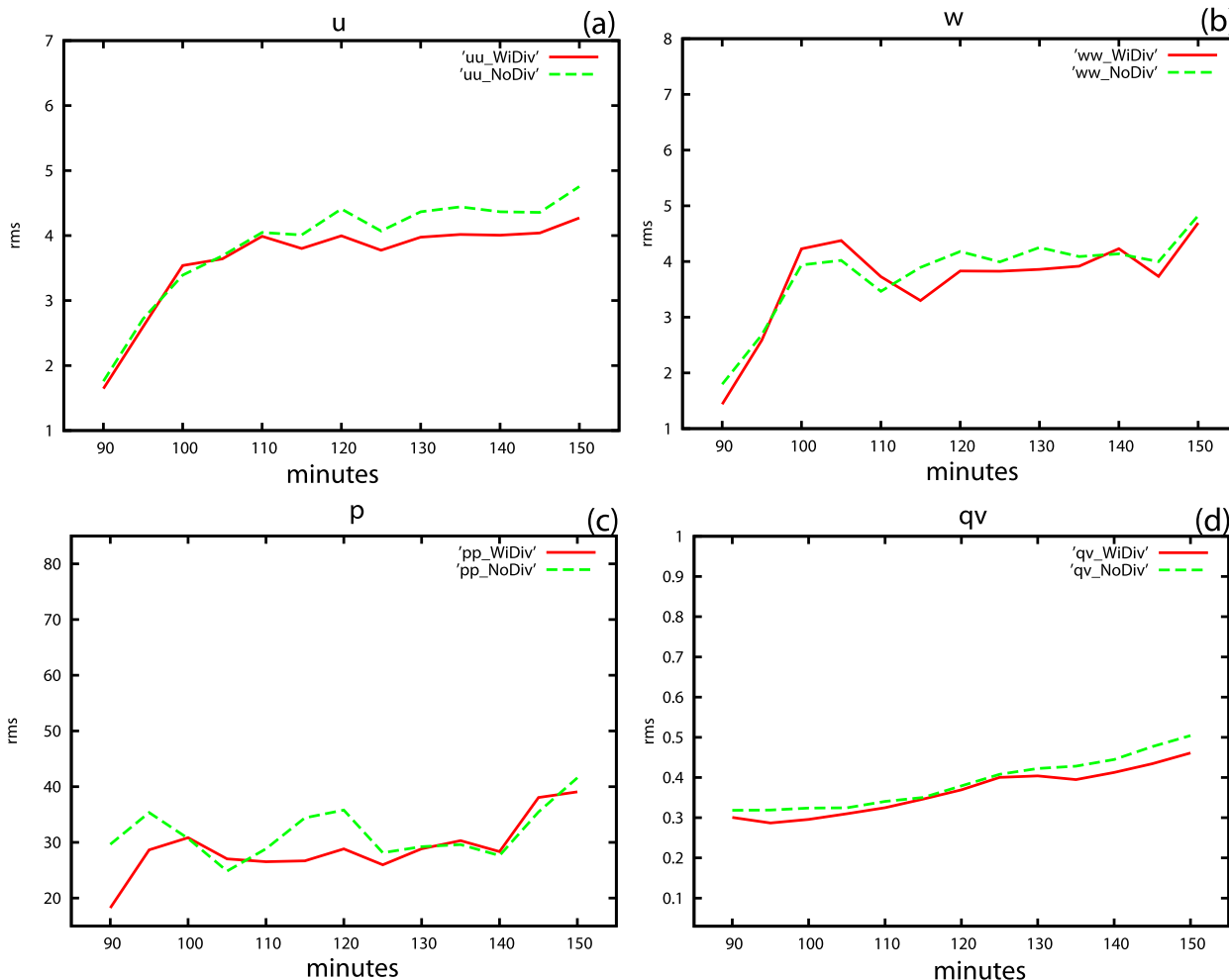


FIG. 7. The rms errors for 1-h forecast after data assimilation cycles with (a) horizontal wind component  $u$  ( $\text{m s}^{-1}$ ); (b) vertical velocity  $w$  ( $\text{m s}^{-1}$ ); (c) perturbation pressure  $p$  (hpa); and (d) water vapor mixing ratio  $q_v$  ( $\text{g kg}^{-1}$ ). Red and green correspond to the experiments with and without mass continuity constraint, respectively.

These two experiments suggest that, as the errors for the radial velocity data are increased, the role of the mass continuity constraint has a larger positive impact on the resulting analysis. This conclusion is further supported by examining the detailed structure of several selected fields (Fig. 9), where the final analysis for the experiment with the constraint is much better than that for the experiment without it. In the experiment with the constraint, though the cold pool is slightly weaker than that in the reference truth, the other features, such as convergence and rotation of low-level winds (Fig. 9a) and midlevel warm core (Fig. 9b), are all quite similar to the truth simulation (Fig. 2). This is in contrast to the experiment without the constraint, where the cold pool is a little stronger (the minimum  $\theta$  is  $-9.9\text{ K}$  vs  $-8.4\text{ K}$  in the reference truth), the outlines of reflectivity depart from the truth simulation, the extension of the midlevel warm

core is shorter and contains some distortion, and the maximum vertical velocity ( $-42\text{ m s}^{-1}$ ) is much larger than found in the truth simulation ( $-28.1\text{ m s}^{-1}$ ; Fig. 9d vs Figs. 9b and 2b).

*c. Sensitivity experiments with several microphysics schemes*

In this section, we perform several experiments to examine the sensitivity of the analysis to the microphysics scheme used in the assimilation. For convective-scale DA, the double-moment microphysics schemes have generally been found to perform better than single-moment schemes for several real-data cases (e.g., Jung et al. 2010; Mansell et al. 2010; Yussouf et al. 2013). For the baseline experiment the single-moment Lin et al. (1983) scheme is used. Here we perform three other sensitivity experiments: one with the 3-ICE scheme

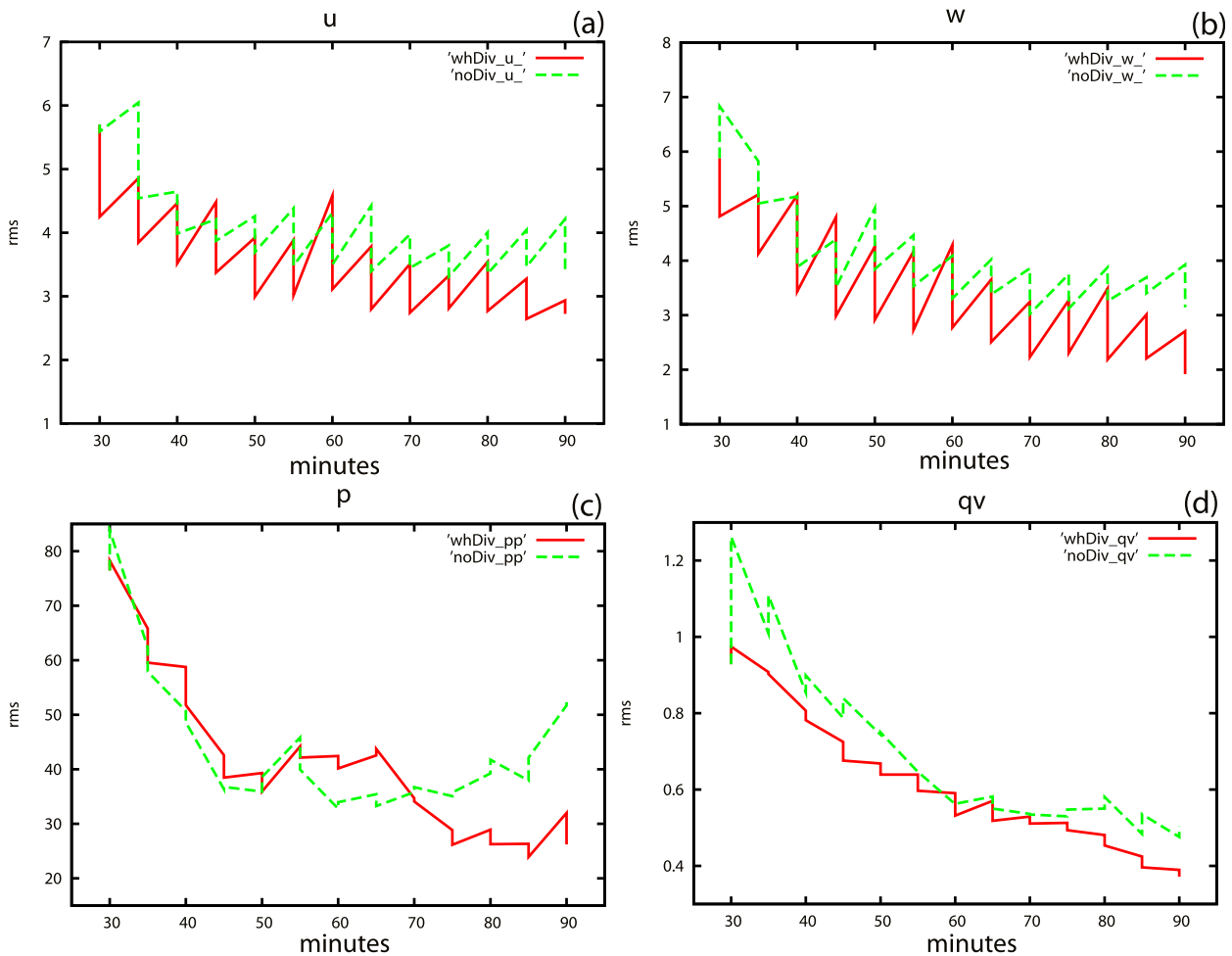


FIG. 8. As in Fig. 4, but for radial velocity observations containing errors of  $5 \text{ m s}^{-1}$ .

(Gilmore et al. 2004), one with the double-moment Milbrandt–Yau scheme, and one with a mixture of all three multiple microphysics schemes, as discussed above.

Figure 10 shows the variations of rms errors for rain-water mixing ratio  $q_r$ , vertical velocity  $w$ , perturbation potential temperature  $\theta'$ , and water vapor mixing ratio  $q_v$ . It is not a surprise that the rms errors for the baseline experiment with the Lin scheme are consistently lowest among all variables because the nature run from which radar observations are derived uses the same Lin scheme. The second-lowest rms errors for the selected variables are from the experiment with the 3-ICE scheme. This is understandable since the 3-ICE scheme is also a single-moment scheme and is quite similar to the Lin scheme. The rms errors for the Milbrandt–Yau scheme are the largest among the experiments, with the errors for  $\theta'$  gradually increasing with the DA cycles going forward (Fig. 10c). Because the Milbrandt–Yau

scheme is very different from the Lin scheme with which the nature run is produced, large model-related systematic errors apparently emerge when the DA cycles are performed. One more experiment with a mixture of the three microphysics schemes is performed to see if these errors can be reduced. As expected, the rms errors are generally larger than those for the two one-moment schemes but smaller than when using just the double-moment Milbrandt–Yau scheme. An examination of the resulting storm structures shows that, in the experiment with the 3-ICE scheme, the low-level cold pool and wind convergence around the storm location is reasonably analyzed (Figs. 11a, 2a), and the midlevel mesocyclone and updraft core look quite similar to those in the nature run (Fig. 11b vs Fig. 2b). The outlines for reflectivity also match the true storm core well. For the experiment with the Milbrandt–Yau scheme, the cold pool is very weak (the minimum perturbation potential temperature is only  $-1.3 \text{ K}$ ). There is no curvature and convergence at

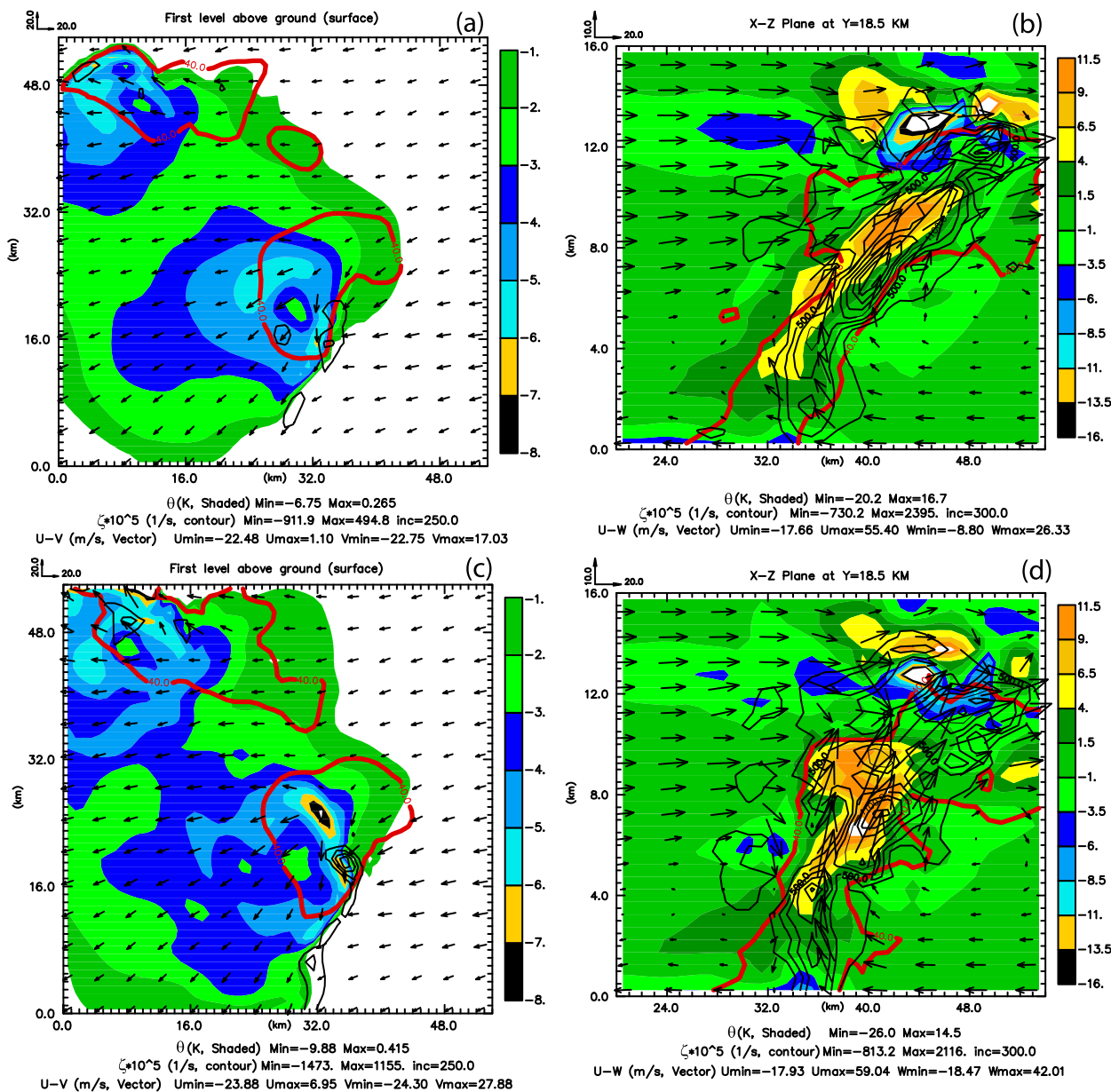


FIG. 9. As in Fig. 3, but for 3DnVAR analysis with radial velocity errors of  $5 \text{ m s}^{-1}$  for the experiments (a),(b) with and (c),(d) without mass continuity constraint. Red solid lines are for reflectivity fields at 40 dBZ.

low levels around the storm near the center of the domain. The area of the midlevel warm core is smaller than in the nature run, although the maximum value for temperature is larger ( $15.7^\circ$  vs  $12.9^\circ$ ). There are nearly parallel stripes of cold and warm anomalies, which contain large bias errors in the upper levels, and a weak spurious center of circulation at the lower-left corner (Fig. 11d) compared to the nature run (Fig. 2b) and other experiments. For the experiment with mixed microphysics schemes, the strength of the cold pool is closer to the nature run but still relatively weak, and its area is too

small (Fig. 11e), but the midlevel mesocyclone and reflectivity structures are well analyzed (Fig. 11f).

There are many different microphysics schemes to choose from, and it is not clear a priori which one will perform best for a given event. Single-moment schemes usually can adequately represent microphysical processes in convective-scale models or CAMs and also have the advantage of being computationally efficient (e.g., Kain et al. 2010). But as the resolution of NWP models increases, the assumptions used in single-moment schemes, especially the particle size distribution, become less valid.

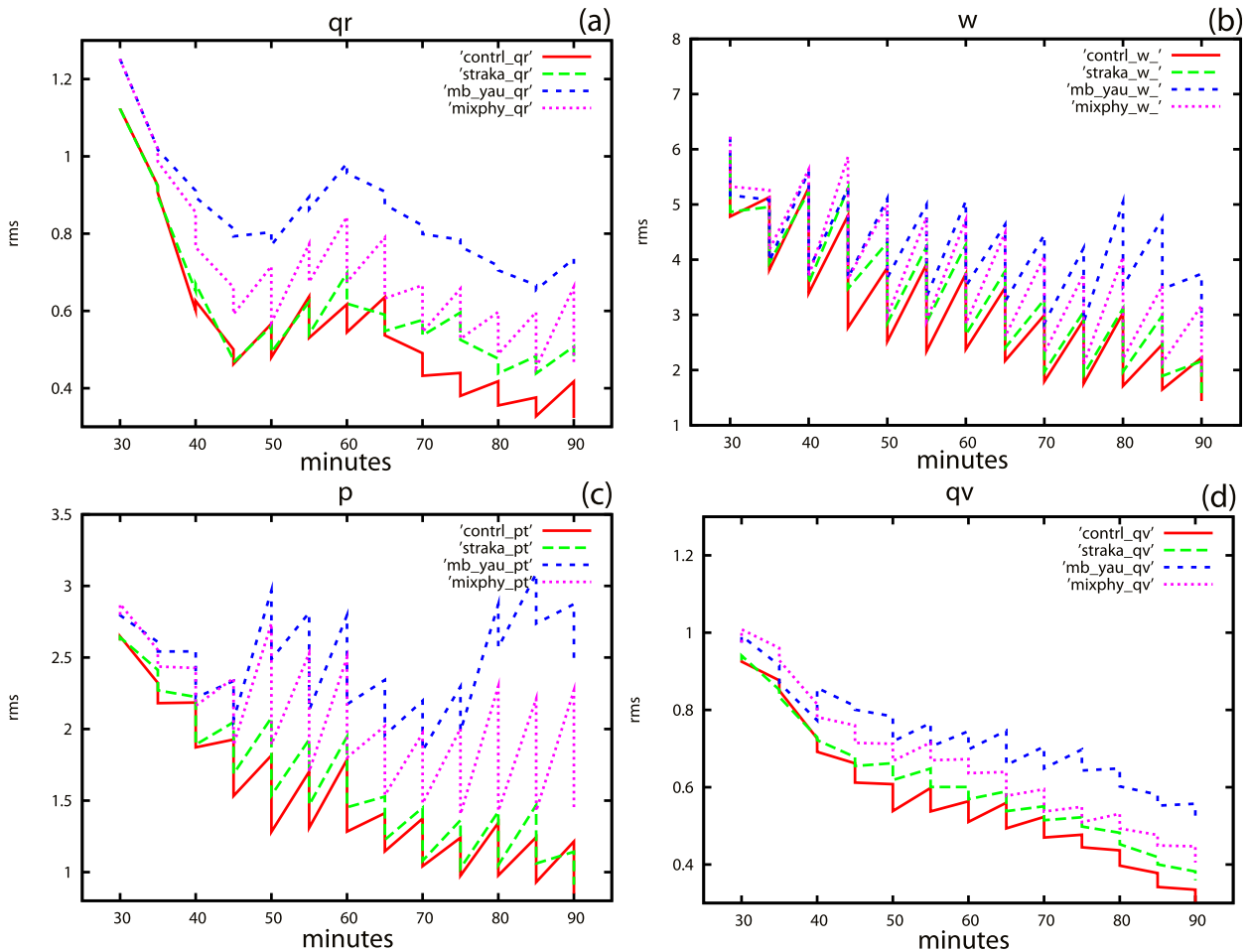


FIG. 10. The rms errors of the analysis and forecast cycles for (a) rainwater mixing ratio  $q_r$  ( $\text{g kg}^{-1}$ ); (b) vertical velocity  $w$  ( $\text{m s}^{-1}$ ); (c) perturbation pressure  $p$  (hPa); and (d) water vapor mixing ratio  $q_v$  ( $\text{g kg}^{-1}$ ). Red, green, blue, and purple lines correspond to the experiments with Lin, Straka 3-ICE, Milbrandt–Yau, and hybrid microphysics schemes, respectively.

Recent results from radar DA cases suggest that double-moment schemes are likely to produce a more realistic reflectivity structure and cold pool strength in a thunderstorm simulation than single-moment schemes (Dawson et al. 2010; Jung et al. 2010). However, a recent study assimilating satellite-retrieved cloud water path showed that the simpler single-moment microphysics schemes can outperform the more complex double-moment schemes (Jones and Stensrud 2015). These contrasting results suggest that there is no consensus regarding which microphysics scheme types are needed for convective-scale NWP. For this reason, ensemble DA and forecasts using multiple microphysics schemes may be a good choice, as model errors related to different microphysics schemes could be reduced.

#### d. Impact of assimilating reflectivity observations

Many previous studies have revealed that the creation of realistic storm precipitation structures early in the

assimilation period results in reduced model spinup time and can be accomplished by assimilating reflectivity observations (Hu et al. 2006; Dowell et al. 2011; Gao and Stensrud 2012). However, as discussed previously, when low values of reflectivity are assimilated, spurious storm cells may appear. Four sensitivity experiments are performed, with three of them assimilating reflectivity values above the thresholds of 5, 15, and 35 dBZ and one assimilating only radial velocity (used for reflectivity values greater than 0 dBZ). It is clearly shown in Fig. 12a that assimilating reflectivity can reduce spinup time, as it decreases rms errors for reflectivity in the first five to six assimilation cycles (first 30 min of assimilation). The rms errors for perturbation pressure  $p$  (Fig. 12c) are also obviously reduced during most of the assimilation period (Fig. 12c). Assimilating reflectivity in general also has a small positive impact on the quality of wind field (e.g., vertical velocity  $w$  in Fig. 12b) and water vapor mixing ratio  $q_v$ . The low threshold reflectivity value of 5 dBZ

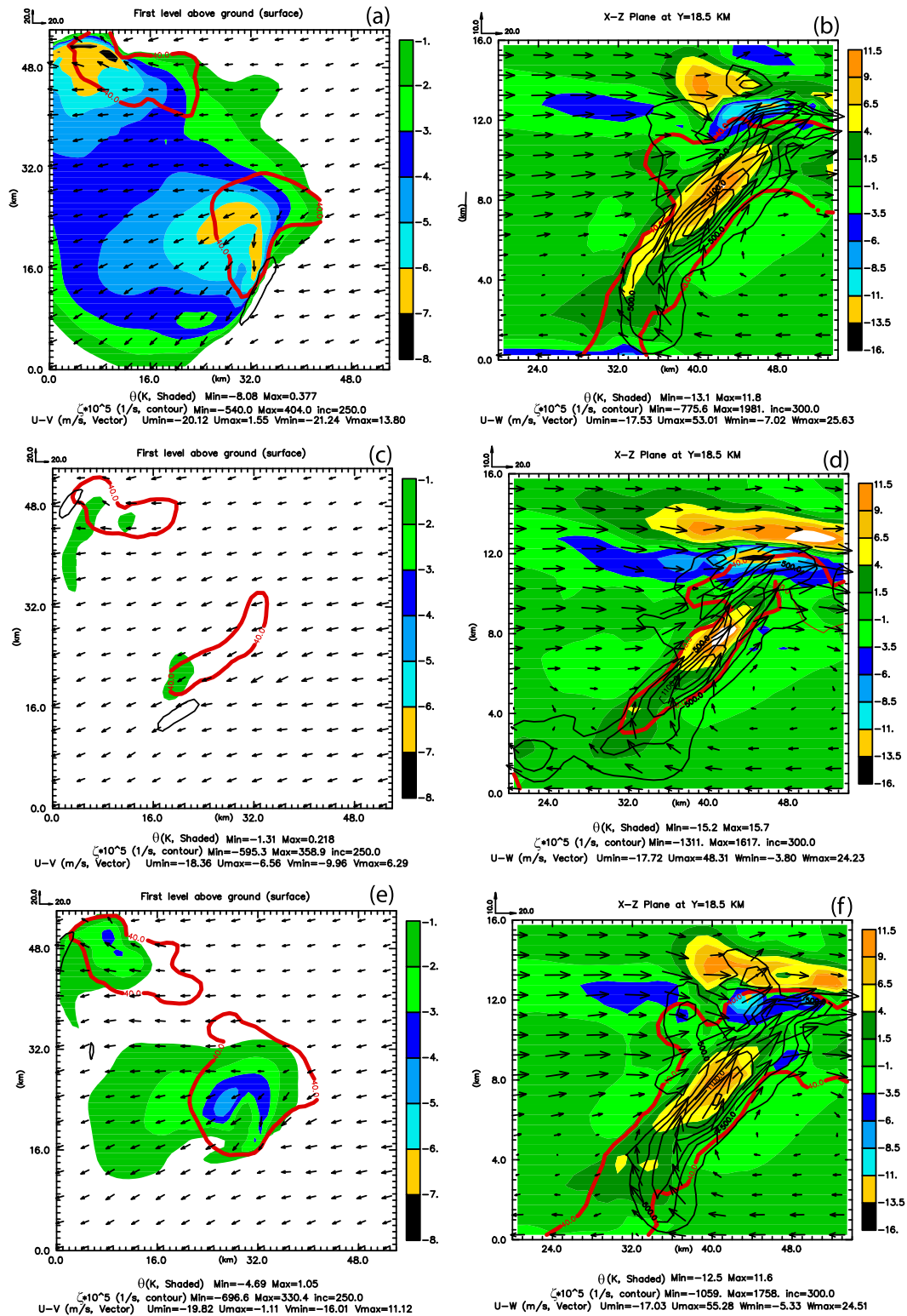


FIG. 11. As in Fig. 3, but for 3DENVAR analysis with several different microphysics schemes. (a),(b) The experiment with the Straka 3-ICE scheme; (c),(d) the experiment with the two-moment Milbrandt-Yau scheme; and (e),(f) the hybrid microphysics schemes. Red solid lines are for reflectivity fields at 40 dBZ.

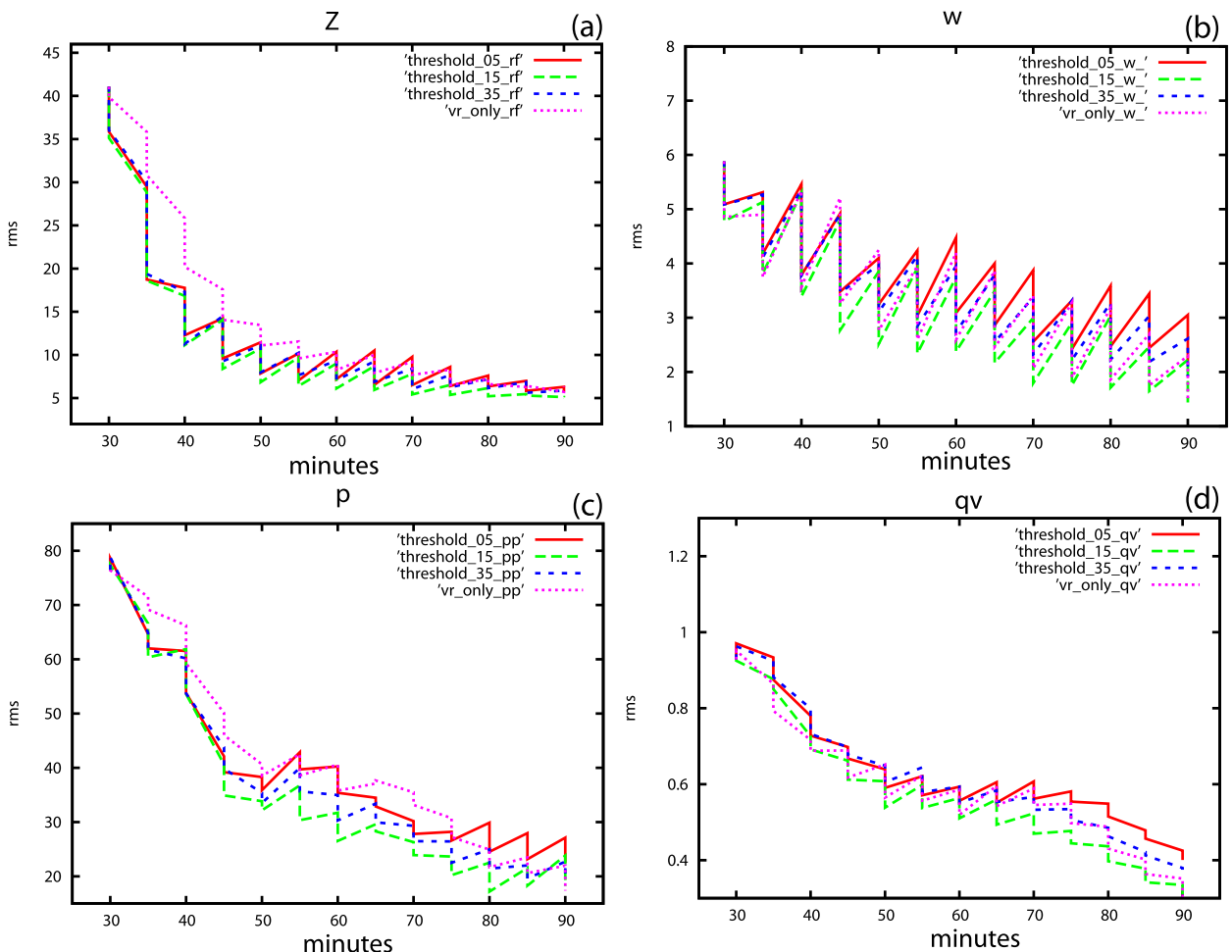


FIG. 12. The rms errors of the analysis and forecast cycles for (a) reflectivity  $Z$  (dBZ), (b) vertical velocity  $w$  ( $\text{m s}^{-1}$ ), (c) perturbation pressure  $p$  (hPa), and (d) water vapor mixing ratio  $q_v$  ( $\text{g kg}^{-1}$ ). Red, green, blue, and purple lines correspond to the experiments with reflectivity thresholds 5, 15, and 35 dBZ and without assimilating reflectivity, respectively.

yields the largest rms errors for all selected model variables, especially for  $w$ . A comparison of all the sensitivity experiments suggests that the experiment with threshold reflectivity value of 15 dBZ provides the lowest rms errors for the selected model variables and is chosen for the En3DA scheme. This result agrees with other research for reflectivity data assimilation (Kong et al. 2011; Gao et al. 2013a).

#### e. Experiment with and without observation perturbations

The final set of experiments tests the sensitivity of the En3DA to randomly perturbing the observations for each ensemble member. Houtekamer and Mitchell (1998) proposed to randomly perturb observations in order to maintain ensemble spread and improve analysis quality. The perturbed observations were produced by adding random noise to the actual observations used in

the DA. Different sets of perturbed observations were used in different ensemble members. Whitaker and Hamill (2002) proposed another ensemble Kalman filter DA called the EnSRF, which does not require the observations to be perturbed for every ensemble member. They demonstrated that the elimination of the sampling error associated with the perturbed observations makes their EnSRF algorithm more accurate than the original type of EnKF methods proposed by Evensen (1994) for the same ensemble size. Bowler et al. (2013) proposed an “ensembles of Vars” type of method, which does not need observation perturbations, based on the deterministic EnSRF introduced by Sakov and Oke (2008). Here we perform three additional experiments with the En3DA method to determine if using perturbed observations for each ensemble member is necessary. As in Houtekamer and Mitchell (1998), the perturbed observations for each 3DEnVAR member analysis are

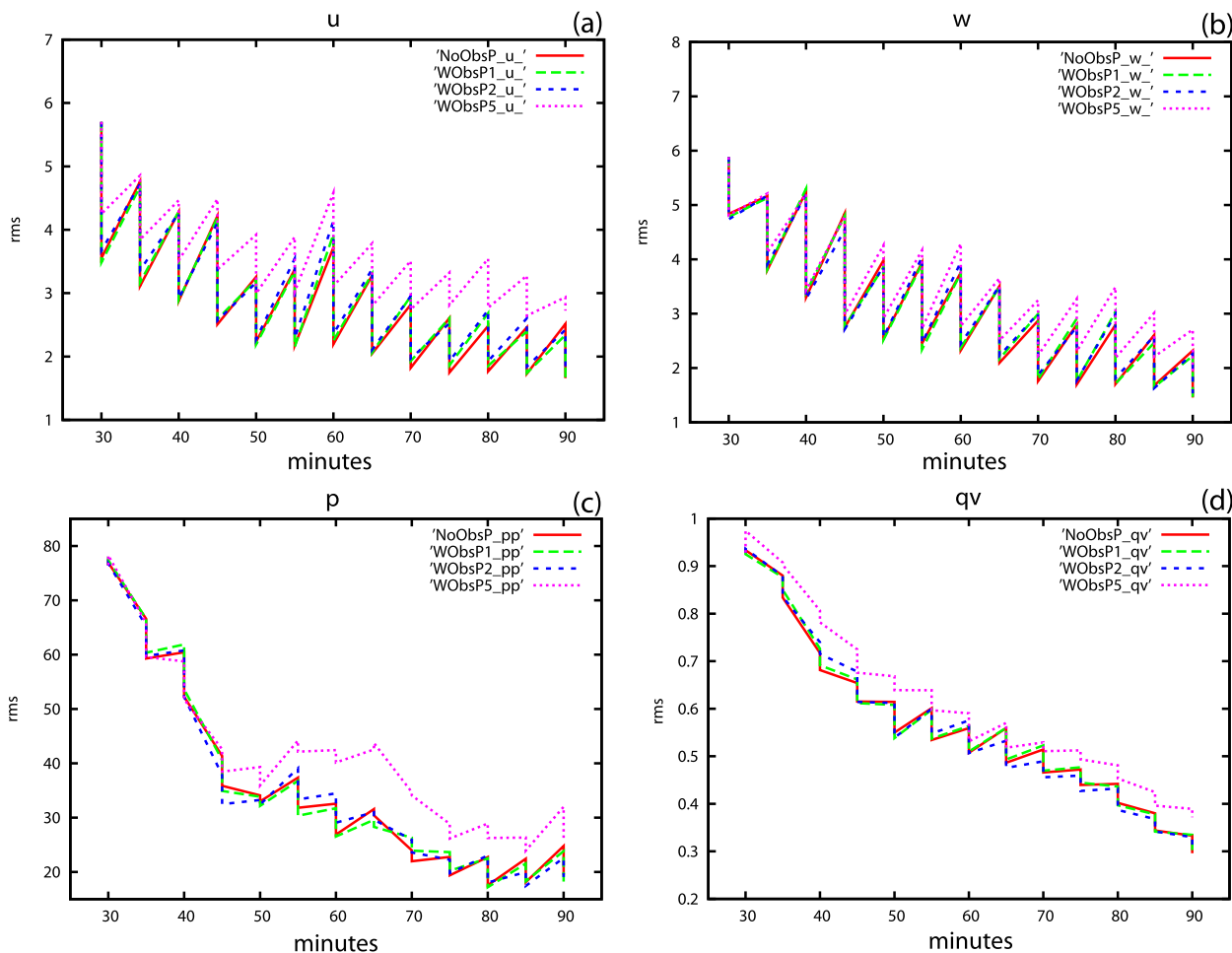


FIG. 13. The rms errors of the analysis and forecast cycles for (a)  $u$  component of wind field ( $\text{m s}^{-1}$ ), (b) vertical velocity  $w$  ( $\text{m s}^{-1}$ ), (c) perturbation pressure  $p$  (hPa), and (d) water vapor mixing ratio  $q_v$  ( $\text{g kg}^{-1}$ ). Red, green, blue, and purple lines correspond to the experiments without observation perturbations and with observation perturbation values of 1, 2, and  $5 \text{ m s}^{-1}$ , respectively.

produced by adding random noise to the radial velocity observations with standard deviations of 1, 2, and  $5 \text{ m s}^{-1}$ , respectively. The results of the three new experiments are compared with the results with the baseline experiment, which has a similar setup, but the same reflectivity and radial velocity observations are used for all ensemble members.

Figure 13 shows that the rms errors for the  $u$  and  $w$  wind components, pressure perturbation  $p$ , and water vapor mixing ratio  $q_v$  are, on average, at similar levels for experiments with noise amplitudes for radial velocity set to 1 and  $2 \text{ m s}^{-1}$  and the baseline experiment without different observation perturbations for each ensemble member. However, in the experiment with random noise amplitudes of  $5 \text{ m s}^{-1}$ , the errors for selected variables  $u$ ,  $p$ , and  $q_v$  are all generally larger than in the other experiments, especially for cycles of DA after 50 min, although the errors for  $w$  are close to those of the other experiments.

Introducing additional perturbations of the radial velocity observations for each ensemble member generally does not help to improve the quality of the DA results and, when the amplitude of perturbation is large enough (with  $5 \text{ m s}^{-1}$  in the radial velocity data), these perturbations actually hurt the quality of the analysis and lead to larger analysis errors. Actually, Fig. 14 shows that the averaged ensemble spreads for several selected variables in all experiments stay quite close to each other during the DA cycles. This indicates that adding random noise to the observations used in the DA for each ensemble member does not improve the accuracy of the analysis for assimilating radar data of this idealized supercell storm.

### 5. Summary and conclusions

In this study, an ensemble of the 3DENVAR system named En3DA has been developed based on the

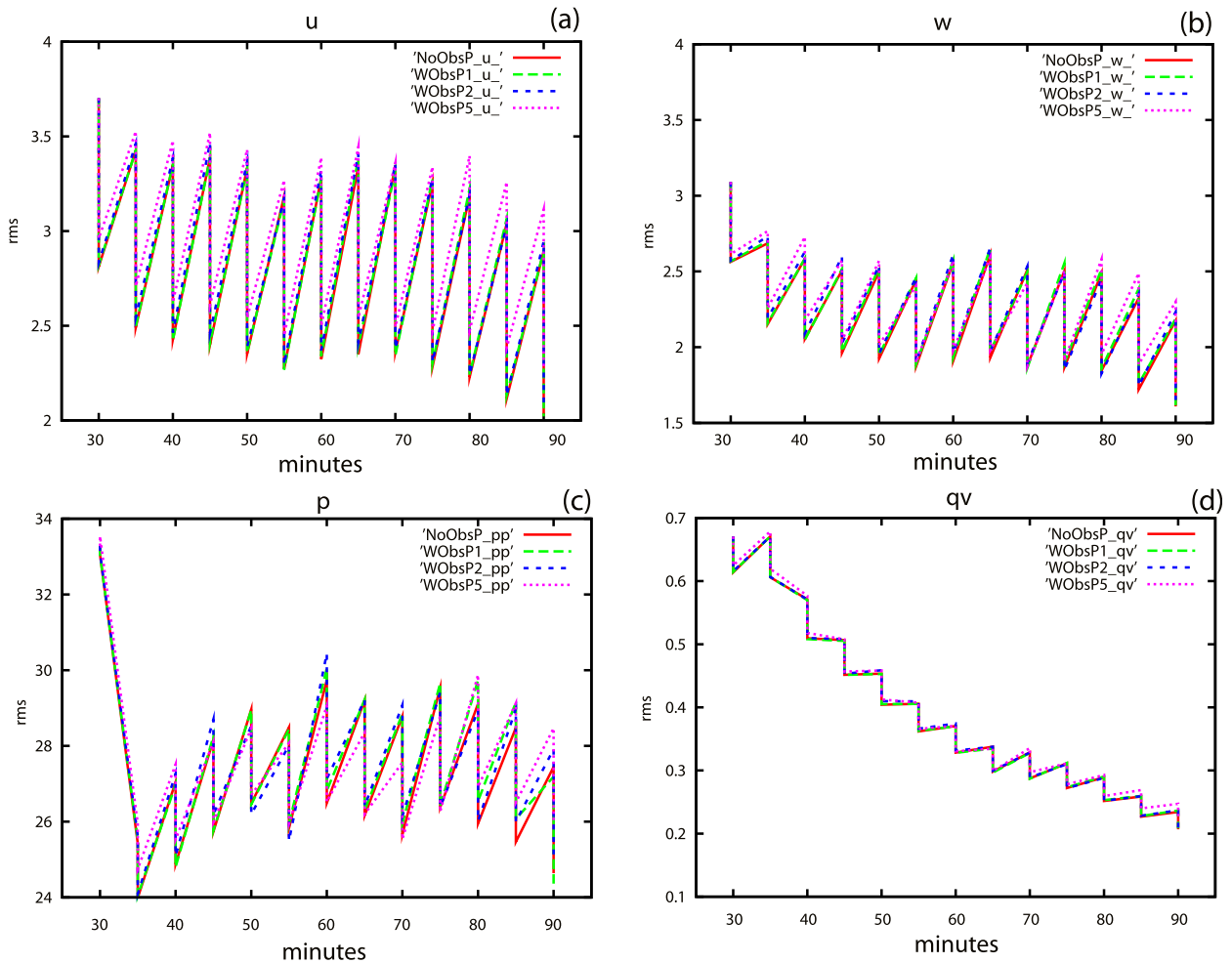


FIG. 14. The evolution of ensemble spread for model variables (a)  $u$  component of wind field ( $\text{m s}^{-1}$ ); (b) vertical velocity  $w$  ( $\text{m s}^{-1}$ ); (c) perturbation pressure  $p$  (hPa); and (d) water vapor mixing ratio  $q_v$  ( $\text{g kg}^{-1}$ ). Red, green, blue, and purple lines correspond to the experiments without observation perturbations and with observation perturbation values of 1, 2, and  $5 \text{ m s}^{-1}$ , respectively.

existing 3DVAR program within the ARPS model. The flow-dependent covariances derived from an ensemble of model forecasts are used in the ensemble of 3DVAR analyses. In addition, extra analysis and forecast cycles are performed for a control member, where the initial condition for the control member is not perturbed at the beginning of the DA cycle. This approach is quite similar to classic ensemble forecasts with a control member and perturbed ensemble members. The method is applied to the assimilation of both radar radial velocity and reflectivity data sampled from a simulated supercell storm.

It is shown in the baseline experiment that the flow-dependent ensemble covariances derived from En3DA and the forecast system lead to the production of quality analyses. Several key features of the simulated storm, including the low-level cold pool, the low-level convergence zone, and the midlevel mesocyclone, are well analyzed.

Several groups of sensitivity experiments are conducted to test the robustness of the method.

Results from the first group of sensitivity experiments demonstrate the benefit of incorporating the mass continuity equation as a weak constraint into the En3DA algorithm. When radial velocity observations contain small errors with amplitudes of  $1 \text{ m s}^{-1}$ , the impact of the mass continuity equation on the analysis is very limited. However, when radial velocity observations contain larger errors with amplitudes of  $5 \text{ m s}^{-1}$ , the quality of the analysis is greatly improved when using the mass continuity constraint, and the general storm features better match the truth simulation.

In the second group of experiments, we examine the sensitivity of the analysis to the microphysics scheme. It is found that DA results are quite sensitive to the microphysics scheme used. Because the truth simulation is created using a single-moment Lin microphysics

scheme, it is no surprise to see that the experiment with the single-moment 3-ICE scheme outperforms the experiment with the double-moment Milbrandt–Yau scheme. In real data cases, it is very hard to know a priori which microphysics scheme will outperform the others, although theoretically double-moment schemes should perform better than single-moment schemes. For this reason, ensemble forecasts with multiple microphysics schemes may be a reasonable choice going forward, as model errors related to the microphysics schemes could be reduced, as also suggested by Yussouf and Stensrud (2010) and Yussouf et al. (2013).

The assimilation of reflectivity observations remains a challenging problem in convective-scale DA. Including reflectivity observations in the assimilation process leads to faster model spinup, although when low values of reflectivity are assimilated, spurious storm cells may be created. Four sensitivity experiments show that assimilating reflectivity can reduce spinup time, as seen by large decreases in rms errors for reflectivity during the first five to six assimilation cycles. Reflectivity assimilation in general also has a small positive impact on the quality of the wind field and water vapor mixing ratio. Among the sensitivity experiments, the experiment with threshold value of 15 dBZ provides the best qualitative analysis and the lowest rms errors. The final group of experiments shows that it is not necessary to perturb radial velocity observations for every ensemble number in order to improve the quality of the analysis.

These results suggest that the incorporation of ensemble-estimated covariance from an ensemble of 3DENVAR DA schemes can help yield a high-quality analysis. The performance is quite similar to the hybrid EnKF and 3DVAR reported in Gao and Stensrud (2014) but is more efficient. This research could have immediate implications for the Warn-on-Forecast (WoF) concept proposed by Stensrud et al. (2009), which envisions a frequently updated numerical model-based probabilistic convective-scale analysis and forecast system to support warning operations within NOAA. Because of the uncertainty related to convective-scale NWP models and the highly chaotic nature of convective weather events, it is essential that ensemble forecasts are utilized in the WoF implementation. However, because of the computational intensity of high-resolution ensemble DA and the resulting forecasts, there are computational challenges to the operational implementation of ensemble Kalman filter and 4DVAR-related algorithms for real-time operations. Results from the current study suggest that the En3DA method is a viable candidate for a WoF system because the background error covariance can be constructed within the method, while the method itself can

be easily implemented with message passing interface and can be very efficient computationally if properly designed. Although the En3DA method has only been tested with OSSEs thus far, future work will focus on real data studies where phase errors will likely appear. In this case, newer verification methods may need to be used. A new interface that links the En3DA method with the more commonly used WRF Model has been developed recently, and we are testing this method in the WRF Model for several real data cases.

*Acknowledgments.* This research was funded by the NOAA Warn-on-Forecast project and NSF Grant AGS-1341878. Chenghao Fu was also partially supported by a research and development fund of Chinese Meteorological Administration for Public Welfare Industrial Meteorology Grant GYHY201306016. The assistance of Dr. Henry Neeman and the University of Oklahoma Supercomputing Center for Education and Research IT team is gratefully acknowledged.

#### REFERENCES

- Barker, D. M., 1999: Var scientific development paper 25: The use of synoptic-dependent error structure in 3DVAR. Met Office Tech. Rep. 2 pp.
- , W. Huang, Y.-R. Guo, A. J. Bourgeois, and Q. Xiao, 2004: A three-dimensional variational data assimilation system for MM5: Implementation and initial results. *Mon. Wea. Rev.*, **132**, 897–914, doi:10.1175/1520-0493(2004)132<0897:ATVDAS>2.0.CO;2.
- , and Coauthors, 2012: The Weather Research and Forecasting Model's Community Variational/Ensemble Data Assimilation System: WRFDA. *Bull. Amer. Meteor. Soc.*, **93**, 831–843, doi:10.1175/BAMS-D-11-00167.1.
- Berre, L., O. Pannekoek, G. Desroziers, S. E. Stefanescu, B. Chapnik, and L. Raynaud, 2007: A variational assimilation ensemble and the spatial filtering of its error covariances: Increase of sample size by local spatial averaging. *Proc. ECMWF Workshop on Flow-Dependent Aspects of Data Assimilation*, Reading, United Kingdom, ECMWF, 151–168.
- Bishop, C. H., D. Hodyss, P. Steinle, H. Sims, A. M. Clayton, A. C. Lorenc, D. M. Barker, and M. Buehner, 2011: Efficient ensemble covariance localization in variational data assimilation. *Mon. Wea. Rev.*, **139**, 573–580, doi:10.1175/2010MWR3405.1.
- Bonavita, M., L. Isaksen, and E. Holm, 2012: On the use of EDA background error variances in the ECMWF 4D-Var. *Quart. J. Roy. Meteor. Soc.*, **138**, 1540–1559, doi:10.1002/qj.1899.
- Bowler, N. E., J. Flowerdew, and S. R. Pring, 2013: Tests of different flavours of EnKF on a simple model. *Quart. J. Roy. Meteor. Soc.*, **139**, 1505–1519, doi:10.1002/qj.2055.
- Buehner, M., 2005: Ensemble-derived stationary and flow-dependent background-error covariances: Evaluation in a quasi-operational NWP setting. *Quart. J. Roy. Meteor. Soc.*, **131**, 1013–1043, doi:10.1256/qj.04.15.
- , P. L. Houtekamer, C. Charette, H. L. Mitchell, and B. He, 2010a: Intercomparison of variational data assimilation and the ensemble Kalman filter for global deterministic NWP.

- Part I: Description and single-observation experiments. *Mon. Wea. Rev.*, **138**, 1550–1566, doi:10.1175/2009MWR3157.1.
- , —, —, —, and —, 2010b: Intercomparison of variational data assimilation and the ensemble Kalman filter for global deterministic NWP. Part II: One-month experiments with real observations. *Mon. Wea. Rev.*, **138**, 1567–1586, doi:10.1175/2009MWR3158.1.
- Calhoun, K. M., T. M. Smith, D. M. Kingfield, J. Gao, and D. J. Stensrud, 2014: Forecaster use and evaluation of real-time 3DVAR analyses during severe thunderstorm and tornado warning operations in the Hazardous Weather Testbed. *Wea. Forecasting*, **29**, 601–613, doi:10.1175/WAF-D-13-00107.1.
- Caya, A., J. Sun, and C. Snyder, 2005: A comparison between the 4DVAR and the ensemble Kalman filter techniques for radar data assimilation. *Mon. Wea. Rev.*, **133**, 3081–3094, doi:10.1175/MWR3021.1.
- Chang, S.-F., Y.-C. Liou, J. Sun, and S.-L. Tai, 2015: The implementation of the ice-phase microphysical process into a four-dimensional Variational Doppler Radar Analysis System (VDRAS) and its impact on parameter retrieval and quantitative precipitation nowcasting. *J. Atmos. Sci.*, **73**, 1015–1038, doi:10.1175/JAS-D-15-0184.1.
- Clark, A. J., and Coauthors, 2012: An overview of the 2010 Hazardous Weather Testbed experimental forecast program spring experiment. *Bull. Amer. Meteor. Soc.*, **93**, 55–74, doi:10.1175/BAMS-D-11-00040.1.
- Clayton, A. M., A. C. Lorenc, and D. M. Barker, 2013: Operational implementation of a hybrid ensemble/4D-Var global data assimilation system at the Met Office. *Quart. J. Roy. Meteor. Soc.*, **139**, 1445–1461, doi:10.1002/qj.2054.
- Courtier, P. E., 1997: Dual formulation of four-dimensional variational assimilation. *Quart. J. Roy. Meteor. Soc.*, **123**, 2449–2461, doi:10.1002/qj.49712354414.
- Dawson, D. T., M. Xue, J. A. Milbrandt, and M. K. Yau, 2010: Comparison of evaporation and cold pool development between single-moment and multimoment bulk microphysics schemes in idealized simulations of tornadic thunderstorms. *Mon. Wea. Rev.*, **138**, 1152–1171, doi:10.1175/2009MWR2956.1.
- Derber, J. C., and A. Rosati, 1989: A global oceanic data assimilation system. *J. Phys. Oceanogr.*, **19**, 1333–1347, doi:10.1175/1520-0485(1989)019<1333:AGODAS>2.0.CO;2.
- Doviak, R. J., and D. S. Zrnić, 1993: *Doppler Radar and Weather Observations*. 2nd ed. Academic Press, 562 pp.
- Dowell, D., F. Zhang, L. J. Wicker, C. Snyder, and N. A. Crook, 2004: Wind and temperature retrievals in the 17 May 1981 Arcadia, Oklahoma, supercell: Ensemble Kalman filter experiments. *Mon. Wea. Rev.*, **132**, 1982–2005, doi:10.1175/1520-0493(2004)132<1982:WATRIT>2.0.CO;2.
- , L. J. Wicker, and C. Snyder, 2011: Ensemble Kalman filter assimilation of radar observations of the 8 May 2003 Oklahoma City supercell: Influences of reflectivity observations on storm-scale analyses. *Mon. Wea. Rev.*, **139**, 272–294, doi:10.1175/2010MWR3438.1.
- Du, J., 2004: Hybrid ensemble prediction system: A new ensembling approach. *Symp. on the 50th Anniversary of Operational Numerical Weather Prediction*, College Park, MD, Amer. Meteor. Soc., P4.2. [Available online at [http://www.emc.ncep.noaa.gov/mmb/SREF/hybrid\\_50thNWP.pdf](http://www.emc.ncep.noaa.gov/mmb/SREF/hybrid_50thNWP.pdf).]
- Evensen, G., 1994: Sequential data assimilation with a nonlinear quasigeostrophic model using Monte Carlo methods to forecast error statistics. *J. Geophys. Res.*, **99**, 10143–10162, doi:10.1029/94JC00572.
- Ferrier, B. S., 1994: A double-moment multiple-phase four-class bulk ice scheme. Part I: Description. *J. Atmos. Sci.*, **51**, 249–280, doi:10.1175/1520-0469(1994)051<0249:ADMMPF>2.0.CO;2.
- Gao, J., and M. Xue, 2008: An efficient dual-resolution approach for ensemble data assimilation and tests with assimilated Doppler radar data. *Mon. Wea. Rev.*, **136**, 945–963, doi:10.1175/2007MWR2120.1.
- , and D. J. Stensrud, 2012: Assimilation of reflectivity data in a convective-scale, cycled 3DVAR framework with hydrometeor classification. *J. Atmos. Sci.*, **69**, 1054–1065, doi:10.1175/JAS-D-11-0162.1.
- , and —, 2014: Some observing system simulation experiments with a hybrid 3D-EnVAR system for storm-scale radar data assimilation. *Mon. Wea. Rev.*, **142**, 3326–3346, doi:10.1175/MWR-D-14-00025.1.
- , M. Xue, A. Shapiro, and K. K. Droegemeier, 1999: A variational method for the analysis of three-dimensional wind fields from two Doppler radars. *Mon. Wea. Rev.*, **127**, 2128–2142, doi:10.1175/1520-0493(1999)127<2128:AVMFTA>2.0.CO;2.
- , —, K. Brewster, and K. K. Droegemeier, 2004: A three-dimensional variational data assimilation method with recursive filter for single-Doppler radar. *J. Atmos. Oceanic Technol.*, **21**, 457–469, doi:10.1175/1520-0426(2004)021<0457:ATVDAM>2.0.CO;2.
- , and Coauthors, 2013a: A realtime weather-adaptive 3DVAR analysis system for severe weather detections and warnings with automatic storm positioning capability. *Wea. Forecasting*, **28**, 727–745, doi:10.1175/WAF-D-12-00093.1.
- , M. Xue, and D. J. Stensrud, 2013b: The development of a hybrid EnKF-3DVAR algorithm for storm-scale data assimilation. *Adv. Meteor.*, **2013**, 512656, doi:10.1155/2013/512656.
- Gaspari, G., and S. E. Cohn, 1999: Construction of correlation functions in two and three dimensions. *Quart. J. Roy. Meteor. Soc.*, **125**, 723–757, doi:10.1002/qj.49712555417.
- Ge, G., and J. Gao, 2007: Latest development of 3DVAR system for ARPS and its application to a tornadic supercell storm. *22nd Conf. on Weather Analysis and Forecasting/18th Conf. on Numerical Weather Prediction*, Park City, UT, Amer. Meteor. Soc., 2B.6. [Available online at [https://ams.confex.com/ams/22WAF18NWP/techprogram/paper\\_124724.htm](https://ams.confex.com/ams/22WAF18NWP/techprogram/paper_124724.htm).]
- , —, K. A. Brewster, and M. Xue, 2010: Effects of beam broadening and earth curvature in radar data assimilation. *J. Atmos. Oceanic Technol.*, **27**, 617–636, doi:10.1175/2009JTECHA1359.1.
- Gilmore, M. S., J. M. Straka, and E. N. Rasmussen, 2004: Precipitation uncertainty due to variations in precipitation particle parameters within a simple microphysics scheme. *Mon. Wea. Rev.*, **132**, 2610–2627, doi:10.1175/MWR2810.1.
- Hamill, T. M., and C. Snyder, 2000: A hybrid ensemble Kalman filter–3D variational analysis scheme. *Mon. Wea. Rev.*, **128**, 2905–2919, doi:10.1175/1520-0493(2000)128<2905: AHEKFF>2.0.CO;2.
- Houtekamer, P. L., and H. L. Mitchell, 1998: Data assimilation using an ensemble Kalman filter technique. *Mon. Wea. Rev.*, **126**, 796–811, doi:10.1175/1520-0493(1998)126<0796: DAUAEK>2.0.CO;2.
- , and —, 2001: A sequential ensemble Kalman filter for atmospheric data assimilation. *Mon. Wea. Rev.*, **129**, 123–137, doi:10.1175/1520-0493(2001)129<0123:ASEKFF>2.0.CO;2.
- Hu, M., and M. Xue, 2007: Impact of configurations of rapid intermittent assimilation of WSR-88D radar data for the 8 May 2003 Oklahoma City tornadic thunderstorm case. *Mon. Wea. Rev.*, **135**, 507–525, doi:10.1175/MWR3313.1.

- , —, J. Gao, and K. Brewster, 2006: 3DVAR and cloud analysis with WSR-88D level-II data for the prediction of Fort Worth, Texas, tornadic thunderstorms. Part II: Impact of radial velocity analysis via 3DVAR. *Mon. Wea. Rev.*, **134**, 699–721, doi:10.1175/MWR3093.1.
- Hunt, B. R., E. J. Kostelich, and I. Szunyogh, 2007: Efficient data assimilation for spatiotemporal chaos: A local ensemble transform Kalman filter. *Physica D*, **230**, 112–126, doi:10.1016/j.physd.2006.11.008.
- Jones, T. A., and D. J. Stensrud, 2015: Assimilating cloud water path as a function of model cloud microphysics in an idealized simulation. *Mon. Wea. Rev.*, **143**, 2052–2081, doi:10.1175/MWR-D-14-00266.1.
- Jung, Y., M. Xue, and G. Zhang, 2010: Simulations of polarimetric radar signatures of a supercell storm using a two-moment bulk microphysics scheme. *J. Appl. Meteor. Climatol.*, **49**, 146–163, doi:10.1175/2009JAMC2178.1.
- Kain, J. S., and Coauthors, 2010: Assessing advances in the assimilation of radar data and other mesoscale observations within a collaborative forecasting–research environment. *Wea. Forecasting*, **25**, 1510–1521, doi:10.1175/2010WAF2222405.1.
- Kalnay, E., H. Li, T. Miyoshi, S.-C. Yang, and J. Ballabrera-Poy, 2007: 4-D-Var or ensemble Kalman filter? *Tellus*, **59A**, 758–773, doi:10.1111/j.1600-0870.2007.00261.x.
- Kong, F., and Coauthors, 2011: CAPS multi-model storm-scale ensemble forecast for the NOAA HWT 2010 spring experiment. *24th Conf. on Weather and Forecasting/20th Conf. on Numerical Weather Prediction*, Seattle, WA, Amer. Meteor. Soc., P.457. [Available online at <https://ams.confex.com/ams/91Annual/webprogram/Paper181680.html>.]
- Kucukkaraca, E., and M. Fisher, 2006: Use of analysis ensembles in estimating flow-dependent background error variances. ECMWF Tech. Memo. 492, 18 pp. [Available online at <http://www.ecmwf.int/sites/default/files/elibrary/2006/10563-use-analysis-ensembles-estimating-flow-dependent-background-error-variances.pdf>.]
- Li, Y., X. Wang, and M. Xue, 2012: Assimilation of radar radial velocity data with the WRF hybrid ensemble–3DVAR system for the prediction of Hurricane Ike (2008). *Mon. Wea. Rev.*, **140**, 3507–3524, doi:10.1175/MWR-D-12-00043.1.
- Lin, Y., P. S. Ray, and K. W. Johnson, 1993: Initialization of a modeled convective storm using Doppler radar–derived fields. *Mon. Wea. Rev.*, **121**, 2757–2775, doi:10.1175/1520-0493(1993)121<2757:IOAMCS>2.0.CO;2.
- Lin, Y.-L., R. D. Farley, and H. D. Orville, 1983: Bulk parameterization of the snow field in a cloud model. *J. Climate Appl. Meteor.*, **22**, 1065–1092, doi:10.1175/1520-0450(1983)022<1065:BPOTSF>2.0.CO;2.
- Liu, C., Q. Xiao, and B. Wang, 2008: An ensemble-based four-dimensional variational data assimilation scheme. Part I: Technical formulation and preliminary test. *Mon. Wea. Rev.*, **136**, 3363–3373, doi:10.1175/2008MWR2312.1.
- , —, and —, 2009: An ensemble-based four-dimensional variational data assimilation scheme. Part II: Observing System Simulation Experiments with Advanced Research WRF (ARW). *Mon. Wea. Rev.*, **137**, 1687–1704, doi:10.1175/2008MWR2699.1.
- Lorenc, A., 2003: The potential of the ensemble Kalman filter for NWP—A comparison with 4D-Var. *Quart. J. Roy. Meteor. Soc.*, **129**, 3183–3204, doi:10.1256/qj.02.132.
- Maddox, R. A., J. Zhang, J. J. Gourley, and K. W. Howard, 2002: Weather radar coverage over the contiguous United States. *Wea. Forecasting*, **17**, 927–934, doi:10.1175/1520-0434(2002)017<0927:WRCOTC>2.0.CO;2.
- Mansell, E. R., C. L. Ziegler, and E. C. Bruning, 2010: Simulated electrification of a small thunderstorm with two-moment bulk microphysics. *J. Atmos. Sci.*, **67**, 171–194, doi:10.1175/2009JAS2965.1.
- Marquis, J., Y. Richardson, P. Markowski, D. Dowell, J. Wurman, K. Kosiba, P. Robinson, and G. Romine, 2014: An investigation of the Goshen County, Wyoming, tornadic supercell of 5 June 2009 using EnKF assimilation of mobile mesonet and radar observations collected during VORTEX2. Part I: Experiment design and verification of the EnKF analyses. *Mon. Wea. Rev.*, **142**, 530–554, doi:10.1175/MWR-D-13-00007.1.
- Milbrandt, J. A., and M. K. Yau, 2005: A multimoment bulk microphysics parameterization. Part II: A proposed three-moment closure and scheme description. *J. Atmos. Sci.*, **62**, 3065–3081, doi:10.1175/JAS3535.1.
- Purser, R. J., W.-S. Wu, D. F. Parrish, and N. M. Roberts, 2003a: Numerical aspects of the application of recursive filters to variational statistical analysis. Part I: Spatially homogeneous and isotropic Gaussian covariances. *Mon. Wea. Rev.*, **131**, 1524–1535, doi:10.1175/1520-0493(2003)131<1524:NAOTAO>2.0.CO;2.
- , —, —, and —, 2003b: Numerical aspects of the application of recursive filters to variational statistical analysis. Part II: Spatially inhomogeneous and anisotropic general covariances. *Mon. Wea. Rev.*, **131**, 1536–1548, doi:10.1175/2543.1.
- Ray, P. S., B. Johnson, K. W. Johnson, J. S. Bradberry, J. J. Stephens, K. K. Wagner, R. B. Wilhelmson, and J. B. Klemp, 1981: The morphology of severe tornadic storms on 20 May 1977. *J. Atmos. Sci.*, **38**, 1643–1663, doi:10.1175/1520-0469(1981)038<1643:TMOSTS>2.0.CO;2.
- Sakov, P., and P. R. Oke, 2008: A deterministic formulation of the ensemble Kalman filter: An alternative to ensemble square root filters. *Tellus*, **60A**, 361–371, doi:10.1111/j.1600-0870.2007.00299.x.
- Smith, P. L., Jr., C. G. Myers, and H. D. Orville, 1975: Radar reflectivity factor calculations in numerical cloud models using bulk parameterization of precipitation processes. *J. Appl. Meteor.*, **14**, 1156–1165, doi:10.1175/1520-0450(1975)014<1156:RRFCIN>2.0.CO;2.
- Smith, T. M., and Coauthors, 2014: Performance of a real-time 3DVAR analysis system in the Hazardous Weather Testbed. *Wea. Forecasting*, **29**, 63–77, doi:10.1175/WAF-D-13-00044.1.
- Snyder, C., and F. Zhang, 2003: Assimilation of simulated Doppler radar observations with an ensemble Kalman filter. *Mon. Wea. Rev.*, **131**, 1663–1677, doi:10.1175//2555.1.
- Stensrud, D. J., and J. Gao, 2010: Importance of horizontally inhomogeneous environmental initial conditions to ensemble storm-scale radar data assimilation and very short range forecasts. *Mon. Wea. Rev.*, **138**, 1250–1272, doi:10.1175/2009MWR3027.1.
- , and Coauthors, 2009: Convective-scale warn-on-forecast system: A vision for 2020. *Bull. Amer. Meteor. Soc.*, **90**, 1487–1499, doi:10.1175/2009BAMS2795.1.
- , and Coauthors, 2013: Progress and challenges with Warn-on-Forecast. *Atmos. Res.*, **123**, 2–16, doi:10.1016/j.atmosres.2012.04.004.
- Sun, J., 2005: Initialization and numerical forecasting of a supercell storm observed during STEPS. *Mon. Wea. Rev.*, **133**, 793–813, doi:10.1175/MWR2887.1.

- , and N. A. Crook, 1997: Dynamical and microphysical retrieval from Doppler radar observations using a cloud model and its adjoint. Part I: Model development and simulated data experiments. *J. Atmos. Sci.*, **54**, 1642–1661, doi:[10.1175/1520-0469\(1997\)054<1642:DAMRFD>2.0.CO;2](https://doi.org/10.1175/1520-0469(1997)054<1642:DAMRFD>2.0.CO;2).
- , and —, 1998: Dynamical and microphysical retrieval from Doppler radar observations using a cloud model and its adjoint. Part II: Retrieval experiments of an observed Florida convective storm. *J. Atmos. Sci.*, **55**, 835–852, doi:[10.1175/1520-0469\(1998\)055<0835:DAMRFD>2.0.CO;2](https://doi.org/10.1175/1520-0469(1998)055<0835:DAMRFD>2.0.CO;2).
- , and —, 2001: Real-time low-level wind and temperature analysis using single WSR-88D data. *Wea. Forecasting*, **16**, 117–132, doi:[10.1175/1520-0434\(2001\)016<0117:RTLLWA>2.0.CO;2](https://doi.org/10.1175/1520-0434(2001)016<0117:RTLLWA>2.0.CO;2).
- , and H. Wang, 2013: Radar data assimilation with WRF 4D-Var. Part II: Comparison with 3D-Var for a squall line over the U.S. Great Plains. *Mon. Wea. Rev.*, **141**, 2245–2264, doi:[10.1175/MWR-D-12-00169.1](https://doi.org/10.1175/MWR-D-12-00169.1).
- , and Coauthors, 2014: Use of NWP for nowcasting convective precipitation: Recent progress and challenges. *Bull. Amer. Meteor. Soc.*, **95**, 409–426, doi:[10.1175/BAMS-D-11-00263.1](https://doi.org/10.1175/BAMS-D-11-00263.1).
- Thompson, T. E., L. Wicker, X. Wang, and C. Potvin, 2014: A comparison between the Local Ensemble Transform Kalman Filter and the Ensemble Square Root Filter for the assimilation of radar data in convective-scale models. *Quart. J. Roy. Meteor. Soc.*, **141**, 1163–1176, doi:[10.1002/qj.2423](https://doi.org/10.1002/qj.2423).
- Tong, M., and M. Xue, 2005: Ensemble Kalman filter assimilation of Doppler radar data with a compressible nonhydrostatic model: OSS experiments. *Mon. Wea. Rev.*, **133**, 1789–1807, doi:[10.1175/MWR2898.1](https://doi.org/10.1175/MWR2898.1).
- Wang, H., J. Sun, X. Zhang, X.-Y. Huang, and T. Auligne, 2013: Radar data assimilation with WRF 4D-Var. Part I: System development and preliminary testing. *Mon. Wea. Rev.*, **141**, 2224–2244, doi:[10.1175/MWR-D-12-00168.1](https://doi.org/10.1175/MWR-D-12-00168.1).
- Wang, X., C. Snyder, and T. M. Hamill, 2007: On the theoretical equivalence of differently proposed ensemble/3D-Var hybrid analysis schemes. *Mon. Wea. Rev.*, **135**, 222–227, doi:[10.1175/MWR3282.1](https://doi.org/10.1175/MWR3282.1).
- , D. M. Barker, C. Snyder, and T. M. Hamill, 2008a: A hybrid ETKF–3DVAR data assimilation scheme for the WRF Model. Part I: Observing system simulation experiment. *Mon. Wea. Rev.*, **136**, 5116–5131, doi:[10.1175/2008MWR2444.1](https://doi.org/10.1175/2008MWR2444.1).
- , —, —, and —, 2008b: A hybrid ETKF–3DVAR data assimilation scheme for the WRF Model. Part II: Real observation experiments. *Mon. Wea. Rev.*, **136**, 5132–5147, doi:[10.1175/2008MWR2445.1](https://doi.org/10.1175/2008MWR2445.1).
- , D. Parrish, D. Kleist, and J. Whitaker, 2013: GSI 3DVar-based ensemble–variational hybrid data assimilation for NCEP Global Forecast System: Single-resolution experiments. *Mon. Wea. Rev.*, **141**, 4098–4117, doi:[10.1175/MWR-D-12-00141.1](https://doi.org/10.1175/MWR-D-12-00141.1).
- Whitaker, J. S., and T. M. Hamill, 2002: Ensemble data assimilation without perturbed observations. *Mon. Wea. Rev.*, **130**, 1913–1924, doi:[10.1175/1520-0493\(2002\)130<1913:EDAWPO>2.0.CO;2](https://doi.org/10.1175/1520-0493(2002)130<1913:EDAWPO>2.0.CO;2).
- Xiao, Q., Y. Kuo, J. Sun, W. Lee, E. Lim, Y. Guo, and D. M. Barker, 2005: Assimilation of Doppler radar observations with a regional 3D-VAR system: Impact of Doppler velocities on forecasts of a heavy rainfall case. *J. Appl. Meteor.*, **44**, 768–788, doi:[10.1175/JAM2248.1](https://doi.org/10.1175/JAM2248.1).
- Xie, Y., S. Koch, J. McGinley, S. Albers, P. E. Bieringer, M. Wolfson, and M. Chan, 2011: A space–time multiscale analysis system: A sequential variational analysis approach. *Mon. Wea. Rev.*, **139**, 1224–1240, doi:[10.1175/2010MWR3338.1](https://doi.org/10.1175/2010MWR3338.1).
- Xue, M., K. K. Droegemeier, and V. Wong, 2000: The Advanced Regional Prediction System (ARPS)—A multiscale nonhydrostatic atmospheric simulation and prediction tool. Part I: Model dynamics and verification. *Meteor. Atmos. Phys.*, **75**, 161–193, doi:[10.1007/s007030070003](https://doi.org/10.1007/s007030070003).
- , and Coauthors, 2001: The Advanced Regional Prediction System (ARPS)—A multiscale nonhydrostatic atmospheric simulation and prediction tool. Part II: Model physics and applications. *Meteor. Atmos. Phys.*, **76**, 143–165, doi:[10.1007/s007030170027](https://doi.org/10.1007/s007030170027).
- , D. Wang, J. Gao, K. Brewster, and K. K. Droegemeier, 2003: The Advanced Regional Prediction System (ARPS), storm-scale numerical weather prediction and data assimilation. *Meteor. Atmos. Phys.*, **82**, 139–170, doi:[10.1007/s00703-001-0595-6](https://doi.org/10.1007/s00703-001-0595-6).
- Yussouf, N., and D. J. Stensrud, 2010: Impact of high temporal frequency phased array radar data to storm-scale ensemble data assimilation using observation system simulation experiments. *Mon. Wea. Rev.*, **138**, 517–538, doi:[10.1175/2009MWR2925.1](https://doi.org/10.1175/2009MWR2925.1).
- , E. R. Mansell, L. J. Wicker, D. M. Wheatley, and D. J. Stensrud, 2013: The ensemble Kalman filter analyses and forecasts of the 8 May 2003 Oklahoma City tornadic supercell storm using single- and double-moment microphysics schemes. *Mon. Wea. Rev.*, **141**, 3388–3412, doi:[10.1175/MWR-D-12-00237.1](https://doi.org/10.1175/MWR-D-12-00237.1).
- Zhang, F., C. Snyder, and J. Sun, 2004: Impacts of initial estimate and observations on the convective-scale data assimilation with an ensemble Kalman filter. *Mon. Wea. Rev.*, **132**, 1238–1253, doi:[10.1175/1520-0493\(2004\)132<1238:IOIEAO>2.0.CO;2](https://doi.org/10.1175/1520-0493(2004)132<1238:IOIEAO>2.0.CO;2).
- , M. Zhang, and J. Poterjoy, 2013: E3DVar: Coupling an ensemble Kalman filter with three-dimensional variational data assimilation in a limited-area weather prediction model and comparison to E4DVar. *Mon. Wea. Rev.*, **141**, 900–917, doi:[10.1175/MWR-D-12-00075.1](https://doi.org/10.1175/MWR-D-12-00075.1).
- Zupanski, M., 2005: Maximum likelihood ensemble filter: Theoretical aspects. *Mon. Wea. Rev.*, **133**, 1710–1726, doi:[10.1175/MWR2946.1](https://doi.org/10.1175/MWR2946.1).
- , and Coauthors, 2006: Initiation of ensemble data assimilation. *Tellus*, **58A**, 159–170, doi:[10.1111/j.1600-0870.2006.00173.x](https://doi.org/10.1111/j.1600-0870.2006.00173.x).